Journal of the Mechanics and Physics of Solids 130 (2019) 56–81

Contents lists available at ScienceDirect

Journal of the Mechanics and Physics of Solids

journal homepage: www.elsevier.com/locate/jmps

Effective behaviour of porous ductile solids with a non-quadratic isotropic matrix yield surface

Lars Edvard Blystad Dæhli[a,*], Odd Sture Hopperstad[a], Ahmed Benallal[b]

[a] Structural Impact Laboratory (SIMLab), Department of Structural Engineering, Norwegian University of Science and Technology (NTNU), NO-7491 Trondheim, Norway

[b] LMT, ENS Paris-Saclay/CNRS/Université Paris-Saclay, 61 Avenue du Président Wilson, 94235 Cachan, France

ARTICLE INFO

Article history:
Received 21 November 2018
Revised 16 April 2019
Accepted 20 May 2019
Available online 21 May 2019

Keywords:
Numerical limit analysis
Third deviatoric stress invariant
Unit cell modelling
Porous plasticity

ABSTRACT

In this study, we examine the macroscopic yielding of isotropic porous ductile solids having a matrix yield function dependent on the second and third deviatoric stress invariants. Numerical limit analyses using a three-dimensional finite element model of a hollow sphere with a Hershey-Hosford matrix yield function are conducted for different shapes of the matrix yield surface and porosity levels. These numerical results are then used to elucidate first-order effects of the third deviatoric stress invariant on the macroscopic yielding and further used as reference data to assess the performance of two porous plasticity models that incorporate effects of the third deviatoric stress invariant using the isotropic non-quadratic Hershey-Hosford yield function. The first model is derived from an upper-bound limit analysis of the hollow sphere representative volume element using the Gurson-Rice trial velocity field, but with a rather general isotropic matrix yield function. The second model is a simple, heuristic extension of the Gurson model incorporating the equivalent stress measure of the Hershey-Hosford yield function.

From the numerical limit analyses, it is found that the contours of the macroscopic yield surface in the deviatoric plane transform from the hexagonal shape of the underlying matrix yield surface to a rounded triangular shape that converges to the circular shape of the Gurson model as the macroscopic stress triaxiality ratio increases. This shape transformation is dependent upon the porosity level. The upper-bound model was found to be in very good agreement with the numerical data for all stress states, shapes of the matrix yield surface, and porosity levels. The heuristic model provides good predictions for low and moderate levels of porosity pertinent to ductile fracture, but the predictions deteriorate when the stress triaxiality ratio and the porosity level increase.

We also address the issue of how representative the spherical unit cell is for the description of real porous solids. To that end, we make comparisons between a space-filling representative volume element in the form of a cubic unit cell with a centric spherical void and the hollow sphere model. These results show that the hollow sphere model generally provides slightly higher values for the yield limits. The shape of the yield loci is similar for the two models in the case of non-quadratic matrix yield surfaces, while the cubic model gives a different shape of the yield loci for low and intermediate stress triaxiality ratios when the von Mises yield function is used for the matrix.

* Corresponding author.
E-mail address: lars.e.dahli@ntnu.no (L.E.B. Dæhli).

https://doi.org/10.1016/j.jmps.2019.05.014

1. Introduction

The yielding and plastic flow of many metal alloys are dependent on the third deviatoric stress invariant (J_3). The yield surface has regions of higher curvature and is thus a non-quadratic function of the stress components. The shape of the yield surface arises from the physical mechanisms of plastic slip in a polycrystal material and depends markedly on the crystallographic texture of the material. However, also materials with random texture exhibit a non-quadratic yield surface. For instance, FCC materials such as aluminium alloys have been shown to be more accurately described by a non-quadratic yield surface even in the case when the material is isotropic (Hosford, 1972, 1996; Lian and Chen, 1991).

Porous plasticity models are traditionally developed based on a representative volume element (RVE) consisting of matrix material and a spherical void, where the matrix material is governed by the von Mises yield function. As the von Mises yield function depends only on the second deviatoric stress invariant (J_2), there is no microscopic dependence of J_3 through the matrix constitutive formulation. However, a slight J_3 dependence still appears on the macroscopic level, i.e. in the homogenized response of the RVE (Benallal et al., 2014; Cazacu and Revil-Baudard, 2015; Cazacu et al., 2013; Leblond and Morin, 2014). This stems from the stress heterogeneity imposed by the voided structure of the RVE. This macroscopic J_3 dependence was indeed eliminated in the classic derivation of the porous plasticity model by Gurson (1977) due to the exclusion of higher-order terms in the Taylor series expansion of the microscopic plastic dissipation function (Benallal et al., 2014; Cazacu et al., 2013; Leblond and Morin, 2014).

3D yield surfaces for a porous material with von Mises and Tresca matrix behaviour were presented in Revil-Baudard and Cazacu (2014a). The yield surfaces were shown to be affected by J_3 for both matrix descriptions, however most severely for the Tresca matrix behaviour, and it was found that the yield surfaces were centro-symmetric. Also, the porosity was seen to be of key importance for how quickly the yield loci changed shape with increasing levels of hydrostatic tension. This study demonstrates the intricate coupling between the stress invariants, the matrix behaviour and the porosity level. Isotropic yield criteria for matrix materials incorporating first-order effects of J_3 based on limit analysis using the Gurson-Rice trial velocity field (Gurson, 1977; Rice and Tracey, 1969) have been considered in recent studies by Cazacu et al. (2014b), Soare (2016) and Benallal (2017, 2018). Cazacu et al. (2014b) adopt the Tresca yield criterion for the matrix material and derive an analytical criterion for a porous solid under axisymmetric loadings. Soare (2016) employs the non-quadratic isotropic yield criterion first proposed by Hershey (1954) and later by Hosford (1972), which we henceforth will refer to as the Hershey-Hosford yield criterion. Benallal (2017, 2018) considers a general isotropic yield criterion for the matrix material, which includes the Hershey-Hosford yield criterion. The studies by Soare (2016) and Benallal (2017, 2018) are not restricted to axisymmetric loading conditions and result in a yield surface for the porous solid that dramatically changes shape in the Π-plane as the stress state changes from predominantly deviatoric to predominantly hydrostatic. More specifically, when the stress state is predominantly deviatoric, the yield surface of the porous solid resembles that of the underlying matrix material. When the magnitude of the hydrostatic stress increases, the contours of the yield surface of the porous solid for given hydrostatic stress states display a rounded triangular shape in the deviatoric plane – an effect that is explicitly shown in the papers by Soare (2016) and Benallal (2017). Moreover, the yield surface displays centro-symmetry, which is a general property for a porous plastic material where the matrix yield function is an even function of the stress state (Cazacu et al., 2019).

Apart from the analytical work utilizing limit analysis, there are also a number of studies that have been devoted to numerical limit analyses. Trillat and Pastor (2005) made a thorough comparison between static (lower bound) and kinematic (upper bound) numerical limit analyses for a hollow sphere RVE and the Gurson model. They conclude that Gurson's criterion is indeed a good approximation. FE limit analyses have also recently been performed by Madou and Leblond (2012) where both ellipsoidal (prolate and oblate) and cylindrical geometries were considered and used to assess their analytical porous plasticity model. The effects associated with an assemblage of voids were studied by Fritzen et al. (2012). In that study, FE simulations of porous materials comprising a random spatial distribution of spherical voids in an elasto-perfect plastic material governed by J_2 flow theory were performed. The authors considered various spatial configurations and evaluated the statistical properties of the unit cell simulations. Interestingly, their results show that an approximation based on a single centered void, as is the case for the hollow sphere model, gives fairly good agreement to a random distribution of voids when the porosity is rather low, which in their study corresponds to a porosity of 1%. This is a rather realistic volume fraction of potentially void-nucleating particles for many structural metals. Moreover, their results show that the predictions of the Gurson model are less accurate for high porosity levels (up to $f = 0.3$ in their study). This is corroborated by the results in Cazacu et al. (2014b) for a Tresca matrix using porosity levels between $f = 0.001$ and $f = 0.04$. Also the particle shape can affect the numerical results, which was studied recently by Keralavarma (2017) using both cubic and spherical voids in numerical FE limit analyses. The study shows that the RVE with a cubic void lowers the resulting plastic limit load; however, only slightly, and the results were qualitatively similar

Other types of matrix yield functions have also been examined in terms of numerical limit analyses. Guo et al. (2008) employed a Drucker-Prager matrix yield function and compared the FE results to their analytical criterion. In a study by Pastor et al. (2010), numerical limit analysis of the hollow sphere model with Coulomb and Drucker-Prager matrix yield surfaces was undertaken and compared to existing analytical models. Thoré et al. (2011) used both von Mises and Drucker-Prager matrix formulations and their study confirms, from a numerical point-of-view, the J_3 dependence of the macroscopic yield surface for the porous plastic solid when the matrix is governed by the von Mises yield criterion. Similar results for a von Mises matrix were obtained by Alves et al. (2014) with an FE model corresponding to a cubic RVE with a centered,

spherical void. A Tresca matrix formulation was employed in axisymmetric FE calculations by Cazacu et al. (2014b) and further extended to full three-dimensional FE simulations in Cazacu et al. (2014a) utilizing a cubic RVE with a centered, spherical void. Pastor et al. (2015) performed numerical limit analyses (both static and kinematic) of a porous material comprising elliptic cylindrical voids embedded in a Coulomb matrix material. To the best knowledge of the authors, no studies have so far considered FE limit analysis using the Hershey-Hosford yield criterion. This yield criterion is of great relevance for polycrystalline solids that are frequently used for industrial applications, e.g. for aluminium alloys that are increasingly employed by the automotive industry and in protective structures. This serves as a key motivation for the current study.

It was shown by Barlat (1987) how the shape of the yield surface for isotropic solids affects the formability of a sheet material deformed under plane stress conditions. Marciniak-Kuczyński analyses (Marciniak and Kuczyński, 1967) were conducted with the Hershey-Hosford yield criterion and it was found that the formability decreased dramatically for biaxial stress states with increasing curvature of the yield surface. Recently, the influence of the yield surface shape on ductile failure by strain localization was investigated by Dæhli et al. (2017b). To this end, numerical simulations with a unit cell that resembles an imperfection band were performed, adopting the Hershey-Hosford yield criterion for the matrix material. In addition, a heuristic extension of the Gurson model that incorporates J_3 dependence via the Hershey-Hosford yield function was proposed and evaluated against unit cell simulations, and then used in localization analyses according to the theoretical framework established by Rice (1976). It was demonstrated by both methods that the shape of the yield surface of the underlying matrix material has a pronounced influence on the onset of strain localization, and the trend is that the strain to failure decreases when the curvature of the yield surface becomes higher. This highlights the importance of including first-order effects of J_3 in porous plasticity models and substantiates the relevance of making a proper assessment of such models.

In this work, finite element simulations of an RVE in the form of a hollow sphere are conducted to evaluate the macroscopic yield surface of a porous solid. Hence, plastic yielding is expressed in terms of stress components that are averaged over the volume of the RVE. Perfect plastic material behaviour governed by the Hershey-Hosford yield criterion and the associative flow rule is adopted for the matrix material to evaluate the macroscopic yield surface numerically. The exponent of the Hershey-Hosford yield function is varied to investigate the influence of the matrix yield surface curvature on the shape of the macroscopic yield surface. It is found that the shape of the macroscopic yield locus in the Π-plane depends markedly on the macroscopic stress triaxiality when the underlying matrix material is J_3 dependent. The numerical results are further used to assess the performance of the two porous plasticity models based on the Hershey-Hosford yield function recently proposed by Benallal (2017) and Dæhli et al. (2017b). It is found that the porous plasticity model by Benallal (2017), which is derived from a rigorous upper-bound limit analysis, is in very good agreement with the RVE simulations. The heuristic porous plasticity model used by Dæhli et al. (2017b) is found to give a reasonable representation of the yield surface for the porosity levels typically found in metal alloys, but it is less accurate than the upper-bound model for high stress triaxiality ratios and high porosity levels.

The notation used throughout the paper is given in Section 2. The constitutive model of the matrix material is presented in Section 3, while Section 4 briefly presents the two porous plasticity models. Section 5 deals with the formulation of the finite element model for the RVE. The results are presented and discussed in Section 6. Concluding remarks are given in Section 7.

2. Notation

We adopt a Cartesian coordinate system (x_1, x_2, x_3) with orthonormal base vectors $(\mathbf{e}_1, \mathbf{e}_2, \mathbf{e}_3)$, and express all tensor components in this coordinate system if nothing else is stated. The Einstein summation convention is used throughout the paper, unless specifically stated otherwise.

The microscopic (or local) stress and strain rate tensors of the matrix material are denoted $\boldsymbol{\sigma} = \sigma_{ij}\mathbf{e}_i \otimes \mathbf{e}_j$ and $\dot{\boldsymbol{\varepsilon}} = \dot{\varepsilon}_{ij}\mathbf{e}_i \otimes \mathbf{e}_j$, respectively. The invariants of the microscopic stress tensor used in this work are the hydrostatic stress (σ_h), the von Mises equivalent stress ($\sigma_\mathrm{eq}^\mathrm{vm}$), and the deviatoric angle (ω). These invariants are expressed as

$$\sigma_\mathrm{h} = \frac{\sigma_{kk}}{3} \tag{1}$$

$$\sigma_\mathrm{eq}^\mathrm{vm} = \sqrt{\frac{3}{2}\sigma'_{ij}\sigma'_{ij}} \tag{2}$$

$$\omega = \frac{1}{3}\arccos\left(\frac{27}{2}\frac{\det(\boldsymbol{\sigma}')}{(\sigma_\mathrm{eq}^\mathrm{vm})^3}\right) \tag{3}$$

where $\boldsymbol{\sigma}' = \left(\sigma_{ij} - \sigma_\mathrm{h}\delta_{ij}\right)\mathbf{e}_i \otimes \mathbf{e}_j$ is the microscopic deviatoric stress tensor and δ_{ij} is the Kronecker delta.

The macroscopic stress and strain rate tensors are defined by averaging their microscopic counterparts over the volume V of the RVE, i.e.

$$\boldsymbol{\Sigma} = \Sigma_{ij}\mathbf{e}_i \otimes \mathbf{e}_j = \frac{1}{V}\int_V \boldsymbol{\sigma}\,\mathrm{d}V \tag{4}$$

$$\dot{\mathbf{E}} = \dot{E}_{ij}\mathbf{e}_i \otimes \mathbf{e}_j = \frac{1}{V}\int_V \dot{\boldsymbol{\varepsilon}}\ \mathrm{d}V \tag{5}$$

where V comprises the volume of the void V_v and the volume of the matrix V_m, viz.

$$V = V_\mathrm{v} + V_\mathrm{m} \tag{6}$$

The invariants of the macroscopic stress tensor are given by

$$\Sigma_\mathrm{h} = \frac{\Sigma_{kk}}{3} \tag{7}$$

$$\Sigma_\mathrm{eq}^\mathrm{vm} = \sqrt{\frac{3}{2}\Sigma'_{ij}\Sigma'_{ij}} \tag{8}$$

$$\Omega = \frac{1}{3}\arccos\left(\frac{27}{2}\frac{\det(\boldsymbol{\Sigma}')}{(\Sigma_\mathrm{eq}^\mathrm{vm})^3}\right) \tag{9}$$

where the prime again refers to the deviatoric part of the tensor. We note that the macroscopic deviatoric angle (Ω) specifies the angle between the projected Σ_1-axis ($\mathbf{m}_1$) and the stress point (P) in the deviatoric plane, as illustrated in Fig. 1(b). The definition of ω for the microscopic stress tensor is completely analogous.

We will also refer extensively to the macroscopic stress triaxiality ratio, which is defined as

$$T = \frac{\Sigma_\mathrm{h}}{\Sigma_\mathrm{eq}^\mathrm{vm}} \tag{10}$$

The finite element (FE) limit analyses will be conducted under proportional macroscopic loading. To this end, the macroscopic stress triaxiality (T) and the macroscopic deviatoric angle (Ω) are kept constant throughout the loading sequence.

The stress tensor decomposes into a deviatoric and a hydrostatic part. The macroscopic principal stress components may consequently be written on a general form using the dimensionless parameters T and Ω, viz.

$$\Sigma_1 = \left(\frac{2}{3}\cos(\Omega) + T\right)\Sigma_\mathrm{eq}^\mathrm{vm} \tag{11a}$$

$$\Sigma_2 = \left(\frac{2}{3}\cos\left(\Omega - \frac{2\pi}{3}\right) + T\right)\Sigma_\mathrm{eq}^\mathrm{vm} \tag{11b}$$

$$\Sigma_3 = \left(\frac{2}{3}\cos\left(\Omega + \frac{2\pi}{3}\right) + T\right)\Sigma_\mathrm{eq}^\mathrm{vm} \tag{11c}$$

We note that these are generally not the ordered principal stress components, since their ordering is exclusively related to the deviatoric angle Ω. However, in the current context, we employ isotropy and the deviatoric angle Ω can then be restricted to $0^\circ \leq \Omega \leq 60^\circ$. Thus, the ordering of the macroscopic principal stresses corresponds to $\Sigma_1 \geq \Sigma_2 \geq \Sigma_3$ in the current study. Fig. 1 provides a graphical interpretation of the stress state parameters used in the sequel.

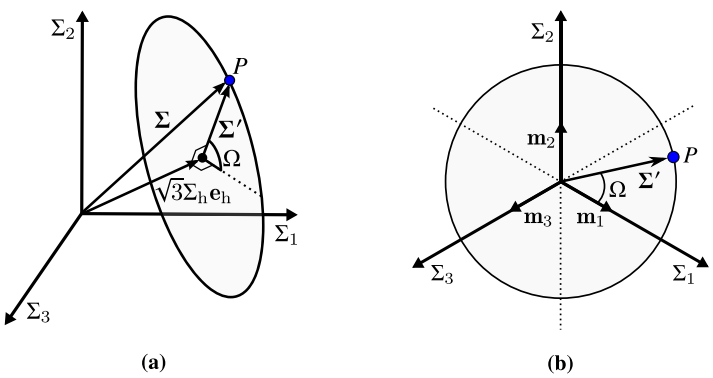

Fig. 1. Illustration of an arbitrary stress point (P) depicted in (**a**) the principal stress space and (**b**) the deviatoric plane. The unit vector $\mathbf{e}_\mathrm{h}$ is directed along the hydrostatic axis and the three vectors $\mathbf{m}_i$ are the projected unit base vectors in the deviatoric plane.

3. Matrix constitutive model

The elastic response of the matrix material is governed by the hypoelastic formulation of the generalized Hooke's law, for which the elastic modulus (E) and the Poisson ratio (ν) are listed in Table 1. We set the Poisson ratio to the rather high value of $\nu = 0.49$ in the numerical calculations to mimic a close-to-incompressible material response also in the elastic domain without introducing numerical stability problems (Madou and Leblond, 2012; 2013; Tekoğlu et al., 2012). This ensures that an incompressible velocity field develops sooner in the FE calculations, which is a prerequisite for the upper-bound limit analysis performed by Gurson (1977).

The plastic response of the matrix material is governed by the Hershey-Hosford non-quadratic isotropic yield function

$$\phi(\boldsymbol{\sigma}) = \sigma_{\text{eq}}(\boldsymbol{\sigma}) - \sigma_0 \leq 0 \tag{12}$$

where the equivalent stress is given by

$$\sigma_{\text{eq}} = \left(\frac{1}{2}\left[(\sigma_{\text{I}} - \sigma_{\text{II}})^m + (\sigma_{\text{I}} - \sigma_{\text{III}})^m + (\sigma_{\text{II}} - \sigma_{\text{III}})^m\right]\right)^{\frac{1}{m}} = \sigma_{\text{eq}}^{\text{vm}} g(\omega) \tag{13}$$

The ordered principal stress components are denoted $\sigma_{\text{I}} \geq \sigma_{\text{II}} \geq \sigma_{\text{III}}$ and m represents the yield surface exponent that dictates the shape of the yield surface. The equivalent stress may be written as a product of the von Mises equivalent stress and a function $g(\omega)$ that depends non-linearly on the deviatoric angle, as indicated by the last equality in Eq. (13). We note that exponent values within the ranges $1 \leq m \leq 2$ and $4 \leq m < \infty$ give yield surfaces lying in-between the von Mises ($m = 2, 4$) and the Tresca ($m = 1, \infty$) yield surfaces. However, the higher range of exponents is more convenient and most frequently used. The exponent values $m = 6$ and $m = 8$ are often associated with BCC and FCC materials, respectively (Hosford, 1996).

The yield stress in uniaxial tension is denoted σ_0 and is constant in this study to conform with the framework of classic limit analysis, which hinges on perfect plastic material behaviour. Further, we adopt the associated flow rule and the plastic strain rate tensor is accordingly given by

$$\dot{\boldsymbol{\varepsilon}}^{\text{p}} = \dot{\lambda}\frac{\partial \phi(\boldsymbol{\sigma})}{\partial \boldsymbol{\sigma}} \tag{14}$$

where $\dot{\lambda} \geq 0$ is the non-negative plastic loading parameter. The matrix yield stress and the yield surface exponent values employed in this study are listed in Table 1. Fig. 2 shows the matrix yield surfaces corresponding to the different yield surface exponents used in the numerical calculations.

A UMAT subroutine available through the material library at the SIMLab (Structural Impact Laboratory) group at NTNU (Norwegian University of Science and Technology) was used in the numerical simulations. The plastic corrections of the elastic trial state were governed by a fully-implicit Backward-Euler stress-update algorithm. We also employed a sub-stepping procedure to ensure that sufficiently small strain increments were used in the plastic iterations. The strain increments sent

Table 1
Overview of the constitutive parameters used for the matrix material in the numerical analyses.

Material parameter	E [MPa]	ν	σ_0 [MPa]	m	χ
Parameter value	100	0.49	1	2, 8, 20	0.1

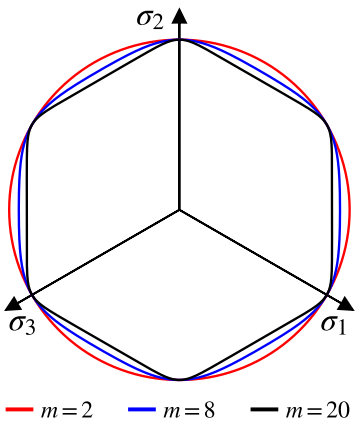

Fig. 2. Matrix yield surfaces for the exponent values used in this study depicted in the deviatoric plane.

to the stress-update algorithm were then governed by $\sqrt{\Delta\boldsymbol{\varepsilon} : \Delta\boldsymbol{\varepsilon}} \leq \chi\sigma_0/E$, where $\Delta\boldsymbol{\varepsilon}$ denotes the total strain increment and χ is a sub-step threshold parameter. In this work, we employ a sub-step threshold parameter value of $\chi = 0.1$. This warrants a rather small strain increment to be used in the plastic correction iterations. We note that the ratio between the yield stress and the elastic modulus was $\sigma_0/E = 0.01$ in all the analyses conducted herein, as inferred from the parameters listed in Table 1, which corresponds to an unusually high yield strain for typical metals. However, this value has no significance for the current study since we are only interested in determining the limit load of the unit cell. As the limit load is attained, i.e. when a sufficient portion of the unit cell behaves perfectly plastic, the macroscopic response is unaffected by elasticity since the stresses have saturated.

4. Porous plasticity models with non-quadratic matrix yield criterion

4.1. Rigorous model developed from upper-bound analysis

We will only make a brief presentation of the porous plasticity model in this section and the reader is referred to the original article for more details (Benallal, 2017). The model has been developed along the same lines as the original Gurson model, with an incompressible, isotropic and rigid-plastic matrix description, using the Gurson-Rice trial velocity field (Gurson, 1977; Rice and Tracey, 1969). However, in contrast to the original Gurson model, plastic yielding of the matrix is now taken to be J_3 dependent and governed by the general relation

$$\phi(\boldsymbol{\sigma}) = \sigma_{\text{eq}} - \sigma_0 = \sigma_{\text{eq}}^{\text{vm}} g(\omega) - \sigma_0 \leq 0 \tag{15}$$

where the microscopic deviatoric angle ($\omega(\boldsymbol{x})$) varies with the position ($\boldsymbol{x}$) throughout the matrix material and generally deviates from the macroscopic counterpart (Ω).

The model can formally be written in the same global expression as the Gurson model, but it involves four functions a, R, P and Q that all depend on the macroscopic stress triaxiality T, the macroscopic deviatoric angle Ω and the porosity f. These functions are generally not available in closed form, but they can be given explicit forms by numerical integration and interpolation of the resulting data. The effective yield surface may then be written on the form (Benallal, 2017)

$$\Phi = \left(\frac{a\Sigma_{\text{eq}}^{\text{vm}} + P}{R\sigma_0}\right)^2 + 2f\cosh\left(\frac{\Sigma_{\text{h}} - Q}{R\sigma_0}\right) - (1 + f^2) = 0 \tag{16}$$

In the current work, we have not focused on evaluating the functions a, R, P and Q. We have rather obtained yield stress values by imposing a multitude of values for the triaxiality and deviatoric angle of the strain rate tensor, which then gives a cloud of yield stress points in terms of T and Ω. Afterwards, the contour plot feature of the Matplotlib library in Python was used to plot the yield surface by interpolation of the yield stress values in the $T - \Omega$ space.

It was shown by Benallal (2017) that when $T \to \infty$, the effective yield point tends towards the hydrostatic point

$$\frac{\Sigma_{\text{h}}}{\sigma_0} = \frac{-\frac{2}{3}\ln f}{g(\frac{\pi}{3})} \tag{17}$$

A similar result is obtained when $T \to -\infty$, which leads to

$$\frac{\Sigma_{\text{h}}}{\sigma_0} = \frac{\frac{2}{3}\ln f}{g(0)} \tag{18}$$

We note that since the Hershey-Hosford yield function is symmetric with respect to $\omega = \frac{\pi}{6}$, we have that $g(0) = g(\frac{\pi}{3})$ and consequently that the magnitude of the hydrostatic stress is equal for $T \to \pm\infty$. For pure shear loading with $\Sigma_{\text{h}} = 0$, it is found that the equation of the yield locus in the Π-plane is given by

$$\Sigma_{\text{eq}}^{\text{vm}} g(\Omega) = (1 - f)\sigma_0 \tag{19}$$

which is equal to the matrix yield function (see Eq. (15)) up to the size reduction factor $1 - f$. However, note that in this case it is the macroscopic deviatoric angle (Ω) that enters the non-linear function g.

In this work, we will focus solely on matrix constitutive behaviour governed by the Hershey-Hosford non-quadratic yield function given in Eq. (12). However, the yield function for the porous plastic material shown in Eq. (16) applies to general types of isotropic J_3-dependent matrix yield functions. Henceforth, we will refer to this model as the upper-bound model or the rigorous model. We note that rigorous here means that the upper bound is obtained in a mathematically rigorous way using the Gurson-Rice trial velocity field, without introducing any simplifying assumptions regarding the microscopic dissipation function. We also note that the modification introduced by Tvergaard (1981) can be employed in the porous plasticity model governed by Eq. (16), which can serve as a means to enhance the predictions in some cases.

4.2. Heuristic extension of the Gurson model

The porous plasticity model developed in the previous section corresponds to the exact solution of the kinematic limit analysis using the Gurson-Rice trial velocity field. Another way to include a J_3 dependence in the Gurson model was presented in Dæhli et al. (2017b) based on the work of Doege and Seibert (1995), where they propose a heuristic extension of the Gurson model to include matrix constitutive behaviour governed by the Hill48 anisotropic yield function. The model used by Dæhli et al. (2017b) preserves the structure of the Gurson yield criterion, viz.

$$\Phi = \left(\frac{\Sigma_{\text{eq}}}{\sigma_0}\right)^2 + 2q_1 f \cosh\left(\frac{3}{2}q_2\frac{\Sigma_{\text{h}}}{\sigma_0}\right) - (1+q_3 f^2) = 0 \tag{20}$$

where the modifications introduced by Tvergaard (1981) have been included since this form is most frequently adopted in the literature. The only difference between the Gurson-Tvergaard model and this heuristic extension is the expression for the macroscopic equivalent stress Σ_{eq}, which is now defined as

$$\Sigma_{\text{eq}} = \left(\frac{1}{2}\left[(\Sigma_{\text{I}}-\Sigma_{\text{II}})^m + (\Sigma_{\text{I}}-\Sigma_{\text{III}})^m + (\Sigma_{\text{II}}-\Sigma_{\text{III}})^m\right]\right)^{\frac{1}{m}} = \Sigma_{\text{eq}}^{\text{vm}} g(\Omega) \tag{21}$$

where $\Sigma_{\text{I}} \geq \Sigma_{\text{II}} \geq \Sigma_{\text{III}}$ are the ordered macroscopic principal stresses. In general, g is a non-linear function of the macroscopic deviatoric angle (Ω), but it is constant and equal to unity for $m = 2, 4$ for which Eq. (20) reduces to the Gurson-Tvergaard model. Throughout this work, we will retain the structure of the original Gurson model and thus set $q_1 = q_2 = q_3 = 1$. We note that Eq. (20) is then exactly the Gurson model, however with the von Mises equivalent stress replaced by the equivalent stress in Eq. (21).

4.3. Comparison between the two porous plasticity models

The yield surfaces obtained by the two porous plasticity models presented in Sections 4.1 and 4.2 through Eqs. (16) and (20) are compared in Fig. 3 for yield surface exponents $m = 2, 8, 20$ and porosity levels $f = 0.001, 0.01, 0.1$. These figures show yield loci for contours of constant hydrostatic stress plotted in the plane spanned by the axes $\Sigma_{\text{eq}}^{\text{vm}}\cos\Omega$ and $\Sigma_{\text{eq}}^{\text{vm}}\sin\Omega$.

It is evident from Fig. 3 that the macroscopic yield surfaces of the two porous plasticity models are nearly identical when the von Mises yield function is used for the matrix material ($m = 2$). The small differences stem from the truncation of the series approximation of the matrix dissipation function in the original Gurson model and are predominantly related to the macroscopic stress triaxiality. It has been shown by Leblond and Morin (2014) that by calculating the second-order approximation of the macroscopic dissipation, the resulting yield surface of the porous solid lies interior to the Gurson model. The porous plasticity model presented in Section 4.1 corresponds to an exact integration of the macroscopic dissipation function, and thus includes this effect of the macroscopic stress triaxiality through the parameters *a, R, P* and *Q* (Benallal et al., 2014). We note that also some effects are associated with J_3, but they are too small to be detected on the yield loci shown in Fig. 3(a)–3(c).

When the yield function of the underlying matrix material is non-quadratic ($m = 8$ and $m = 20$), the shape of the yield surface of the two porous plasticity models is markedly different for non-zero hydrostatic stress. The rigorous upper-bound model gives a yield surface that evolves from the $\pi/6$-type symmetry (hexagonal shape) to the $\pi/3$-type symmetry (rounded triangular shape) as the hydrostatic stress increases, whereas the heuristic model retains the $\pi/6$-type symmetry (hexagonal shape) of the underlying matrix yield function for all levels of hydrostatic stress. This is readily seen from the yield function expressed in Eq. (20); when the hydrostatic stress is constant, the yield function is governed by the equivalent stress, which corresponds to the Hershey-Hosford yield criterion. We note that the rounded triangular shape displayed by the rigorous model leads to a higher yield stress in generalized compression than in generalized tension for the positive hydrostatic stress levels shown in Fig. 3. This effect is opposite for negative hydrostatic stress levels, such that the yield stress in generalized tension is higher than in generalized compression, because the yield functions plotted in Fig. 3 are centro-symmetric (Cazacu et al., 2019).

The yield loci of the rigorous upper-bound model usually lie interior to the yield loci given by the heuristic model, and thus represents a tighter upper-bound solution to the limit analysis in most cases. However, exceptions to this pertain to stress states close to generalized shear ($\Omega = 30^\circ$) when the hydrostatic stress level is rather low, but different from zero. With a keen eye, this can be observed in Fig. 3(g)–3(i) for the contours corresponding to $\Sigma_{\text{h}} = 3.5,\ 2.0$, and 0.9, respectively.

The heuristic model and the rigorous upper-bound model coincide in the Π-plane ($\Sigma_{\text{h}} = 0$), and also at the hydrostatic limits (both compressive and tensile) in the case of the Hershey-Hosford model considered here. However, note that while the former holds in the general case, the latter does not, since the heuristic model always leads to the Gurson hydrostatic limits, while the rigorous model gives the limits shown in Eqs. (17) and (18). These limits are exact for the hollow sphere RVE with general non-quadratic isotropic matrix yield functions (see Benallal, 2018). In the case of the Hershey-Hosford model, we have that $g(0) = g(\pi/3) = 1$, and the two limits coincide.

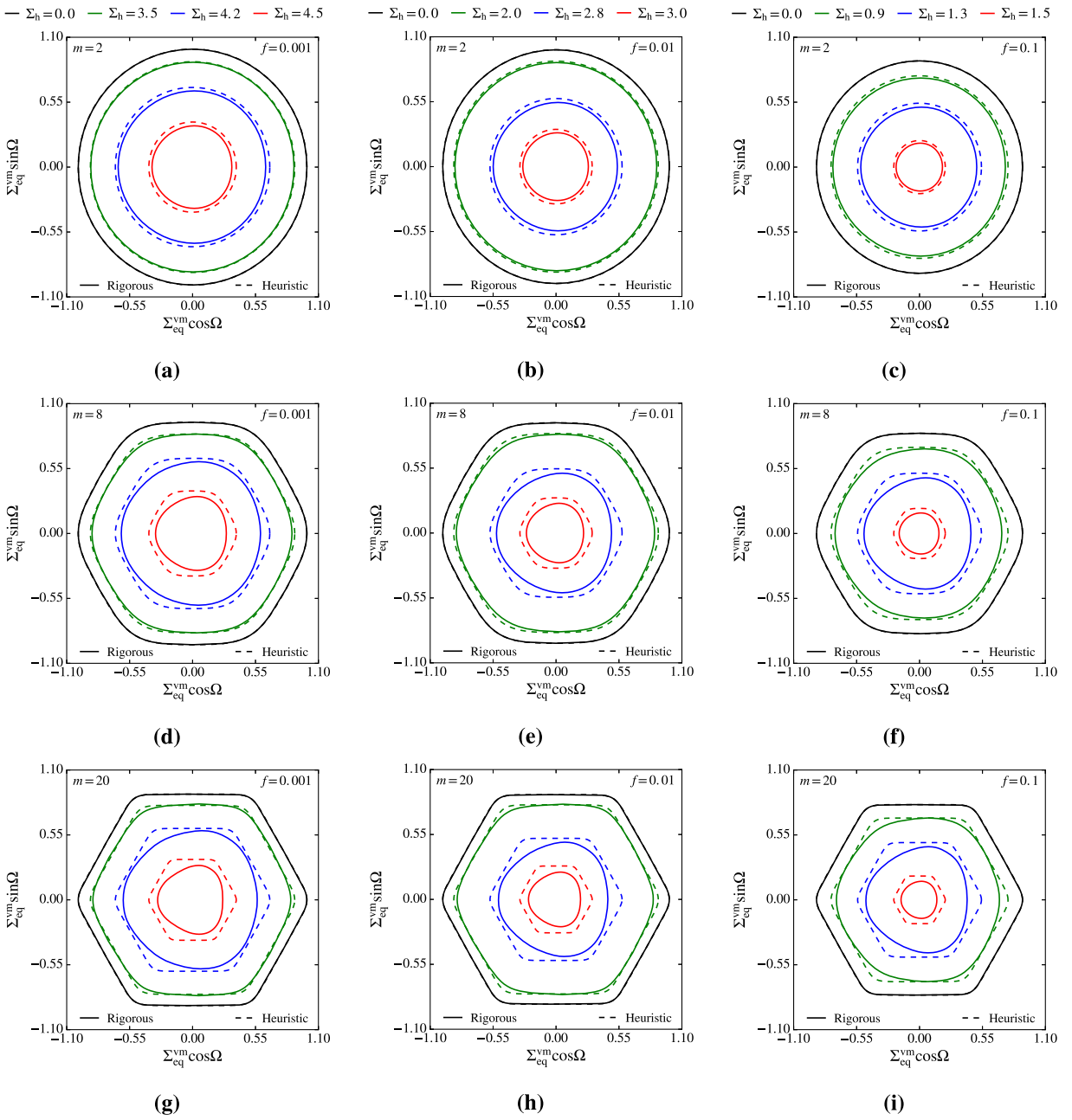

Fig. 3. Comparison between yield surfaces resulting from the rigorous model (solid lines) and the heuristic model (dashed lines) for different yield surface exponents; (**a**)–(**c**) $m = 2$, (**d**)–(**f**) $m = 8$, and (**g**)-(**i**) $m = 20$. The contours represent yield loci for constant levels of hydrostatic stress ($\Sigma_h = \text{cnst}$).

5. Finite element model

5.1. Overview of the finite element model

The RVE used in the FE analyses corresponds to a hollow sphere, in accordance with the Gurson model formulation. We employ symmetry conditions in the three mutually orthogonal directions x_1, x_2, and x_3. Hence, only one-eighth of the RVE is explicitly considered in the FE model, as illustrated in Fig. 4. One of the three symmetry planes (with normal in the x_3-direction) is highlighted with a blue colour in Fig. 4, while the two other symmetry planes (with normals along the x_1-direction and x_2-direction) are not shown. The outer surface of the hollow sphere (highlighted with a dark red colour) is subjected to kinematic boundary conditions, while the void surface (indicated by white colour) is traction-free. In this

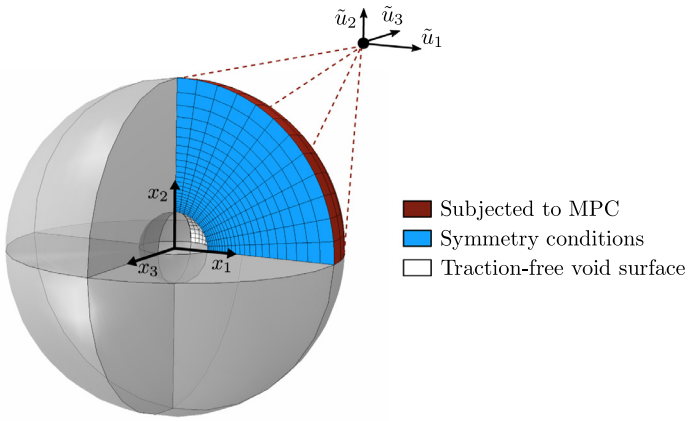

Fig. 4. An illustration of the FE model of the hollow sphere. Symmetry conditions in the three orthogonal directions x_1, x_2, and x_3 are imposed. This is indicated by the internal surfaces with a blue colour. The outer surface is subjected to kinematic boundary conditions, while the void surface is traction-free and free to deform. (For interpretation of the references to colour in this figure legend, the reader is referred to the web version of this article.)

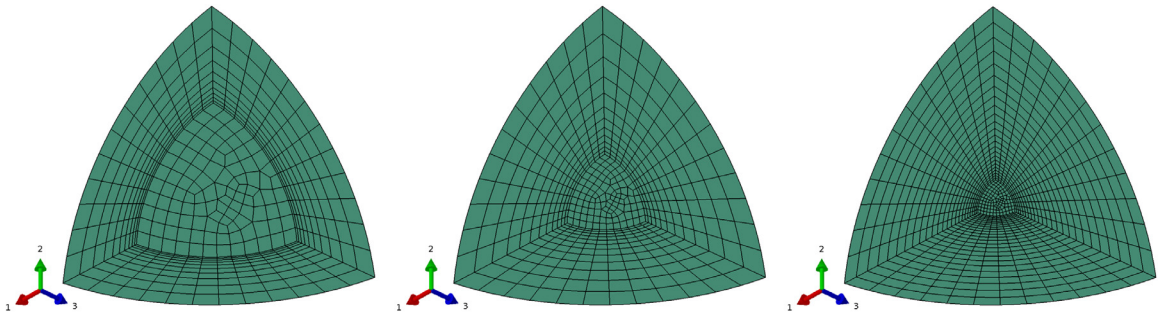

Fig. 5. FE mesh for the hollow sphere model with porosity levels (a) $f = 0.1$, (b) $f = 0.01$, and (c) $f = 0.001$.

work, we have performed FE simulations for three different porosity levels (void volume fractions) that correspond to $f = 0.001, 0.01, 0.1$ and the resulting FE models are shown in Fig. 5.

The undeformed configuration is used as the reference for the numerical computations to conform with the upper-bound limit analysis framework, which is based on small deformation theory. Thus, we do not distinguish between the current and reference configurations in the following. The velocity field imposed to the exterior boundary of the RVE reads

$$\dot{\mathbf{u}} = \dot{\mathbf{E}} \cdot \mathbf{x} \tag{22}$$

where $\dot{\mathbf{E}}$ denotes the homogeneous macroscopic strain rate and $\mathbf{x} = r\mathbf{e}_r$ refers to an arbitrary position on the outer surface of the hollow sphere.

The kinematic boundary conditions governed by Eq. (22) are prescribed such that the macroscopic stress triaxiality (T) and the macroscopic deviatoric angle (Ω) remain constant. The proportional loading is enforced using a method that was first proposed by Faleskog et al. (1998) in a plane-strain setting and later extended to general three-dimensional analyses by Kim et al. (2004). A recent paper by Liu et al. (2016) elaborates on the mathematical details and presents a general unitary transformation matrix that can be implemented in an FE model. The formulation adopted herein is a special case of the general transformation matrix (Liu et al., 2016) and was presented in detail by Dæhli et al. (2017a). For the sake of brevity, we only present the final form of the kinematic constraint equations. These are quite generally written on the form

$$\dot{u}_i = x_i \sum_{k=1}^{3} Q_{ik}(T, \Omega)\dot{\tilde{u}}_k \tag{23}$$

where x_i label positions on the outer surface, $Q_{ik}(T, \Omega)$ are the components of an orthogonal transformation matrix that explicitly depends upon the macroscopic stress triaxiality and the macroscopic deviatoric angle, and $\tilde{u}_k$ are the displacement components in a fictitious system. Note that the Einstein summation convention is abandoned in Eq. (23). The fictitious system is in the sequel referred to as a dummy node due to the use of an external node (reference point in Abaqus) to include these degrees-of-freedom in the FE model. The constraints given in Eq. (23) relate the global displacements of the unit cell model to the dummy node. The boundary conditions are then prescribed such that $\dot{\tilde{u}}_1 > 0$, while the two remaining displacements $\tilde{u}_2$ and $\tilde{u}_3$ remain unspecified to accommodate zero forces in the $\tilde{x}_2$ and $\tilde{x}_3$ directions, respectively.

As a side note, we mention that the MPC user subroutine is actually not needed for these particular analyses since the undeformed geometry is used as the reference configuration. The kinematic constraints given by Eq. (23) are consequently linear and can be imposed directly using linear constraints through the *EQUATION keyword in Abaqus. However, a verified and validated MPC user subroutine was already available and was the preferred option for the numerical simulations conducted herein.

The macroscopic stress state attained in the limit analysis is evaluated from the results files (.odb) by direct calculation of the volume average, viz.

$$\boldsymbol{\Sigma} = \frac{1}{V}\sum_{k=1}^{N_{\text{ip}}} \boldsymbol{\sigma}_k V_k \tag{24}$$

where V is the total volume of the unit cell, V_k and $\boldsymbol{\sigma}_k$ are the volume and the local stress tensor of integration point k, and N_{ip} denotes the total number of integration points. Subsequently, the von Mises equivalent stress and the hydrostatic stress are evaluated from

$$\Sigma_{\text{eq}} = \sqrt{\frac{3}{2}\boldsymbol{\Sigma}' : \boldsymbol{\Sigma}'} \qquad \Sigma_{\text{h}} = \frac{1}{3}\text{tr}(\boldsymbol{\Sigma}) \qquad \boldsymbol{\Sigma}' = \boldsymbol{\Sigma} - \Sigma_{\text{h}}\mathbf{1} \tag{25}$$

where $\mathbf{1}$ is the second-order identity tensor.

5.2. Remarks on the FE mesh

The three different models corresponding to the porosity levels $f = 0.001$, $f = 0.01$, and $f = 0.1$ were spatially discretized using 2520, 1260, and 1050 elements in total, respectively. These configurations correspond to the unit cells shown in Fig. 5. The elements employed were quadratic brick elements with reduced integration (C3D20R in Abaqus/Standard). A mesh refinement study was initially conducted to ensure that the limit load attained in the numerical calculations had converged. To that end, we examined three different element types, namely linear brick elements with reduced (C3D8R) and selectively-reduced (C3D8) integration, and quadratic brick elements with reduced integration (C3D20R). We also limited the mesh refinement study to an RVE comprising a void volume fraction of $f = 0.01$ using the quadratic matrix material ($m = 2$) and a stress state corresponding to $T = 1$ and $\Omega = 0^\circ$. In the final calculations, we chose a slightly more refined mesh than was found necessary for convergence from this mesh refinement study.

Fig. 6 shows the convergence of the limit load for various spatially discretized unit cell configurations. The number of elements along the void edges and the number of elements along the ligament between the void and the outer surface (void/ligament) correspond to (i) 6/10, (ii) 8/12, (iii) 10/15, (iv) 13/20, and (v) 20/30. This led to a total number of 260, 516, 1020, 2560, and 9330 elements, respectively. We note that a seeding bias ratio of 10 was used along the ligament edges, such that the element "height" decreases monotonically in the radial direction towards the void surface. This is inferred from Fig. 5. We readily perceive from Fig. 6 that the quadratic elements give converged results much sooner than the linear elements (both with reduced and selectively-reduced integration). Consequently, the quadratic brick element (C3D20R) was our preferred choice for the analyses conducted herein.

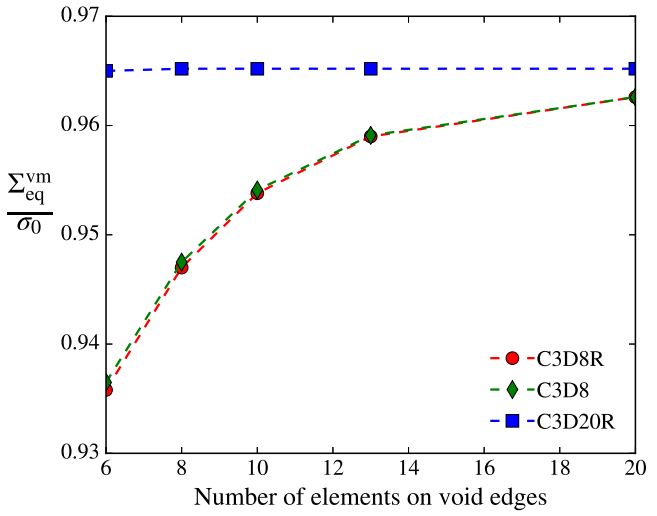

Fig. 6. Convergence rate of the limit load in terms of normalized von Mises equivalent stress ($\Sigma_{\text{eq}}/\sigma_0$) evaluated from a mesh refinement study. The unit cell configuration corresponds to $f = 0.01$ and the loading state to $T = 1$ and $\Omega = 0^\circ$ in the case of a von Mises matrix ($m = 2$).

5.3. Imposed macroscopic stress states

We have assigned a rather large number of stress states in this work to map up the numerical yield surfaces. The imposed loading conditions correspond to stress triaxiality levels of $T = 0,\ 1/4,\ 1/2,\ \pm 1,\ \pm 2,\ \pm 10,\ 50$ and deviatoric angles of $\Omega = 0^\circ,\ 5^\circ,\ 10^\circ, \ldots, 60^\circ$. This yields 130 different stress states for every combination of yield surface exponent and unit cell configuration and the total number of analyses conducted for the current work then amounts 1170. Even though the analyses are individually rather cheap due to the low number of elements and the exclusion of nonlinear geometry in the simulations, they collectively represent a quite exhaustive computational effort. Also, the use of a UMAT subroutine and the non-quadratic matrix yield surface both increase the computational time for the analyses. We therefore decided to only include three negative stress triaxiality ratios, which is deemed sufficient to elucidate the differences between the yield surfaces obtained for negative and positive hydrostatic stress states.

6. Results and discussion

6.1. FE results

Fig. 7 shows the numerical yield limits of the hollow sphere model with a porosity of $f = 0.01$ in terms of the normalized macroscopic von Mises equivalent stress ($\Sigma_{eq}^{vm}/\sigma_0$) against the macroscopic deviatoric angle (Ω). The results pertain to the full range of deviatoric angles imposed to the FE model. Results for all the three different yield surface exponent values are shown and the data points are labelled by a red dot for $m = 2$, a green diamond for $m = 8$, and a blue square for $m = 20$. The figures correspond to (a) $T = -10$, (b) $T = -1$, (c) $T = 0$, (d) $T = 1$, (e) $T = 2$, and (f) $T = 10$.

From Fig. 7(c) we readily observe that the shape of the yield surface corresponds to the underlying matrix yield surface in the case of a purely deviatoric loading state. However, the yield limits are reduced by a factor that scales with the porosity. When the stress triaxiality increases, the yield strength is greater in generalized compression ($\Omega = 60^\circ$) than in generalized tension ($\Omega = 0^\circ$). This observation is readily made from Fig. 7(d)–7(f) and applies to all the yield surface exponents. The opposite trend is observed for negative stress triaxialities, i.e. the yield strength is greater for generalized tension than for generalized compression, which is inferred from Fig. 7(a) and 7(b). This effect causes a six-fold symmetry of the macroscopic yield surface with respect to the stress state and entails that the symmetry around $\Omega = 30^\circ$, which applies to the matrix yield surface, is lost.

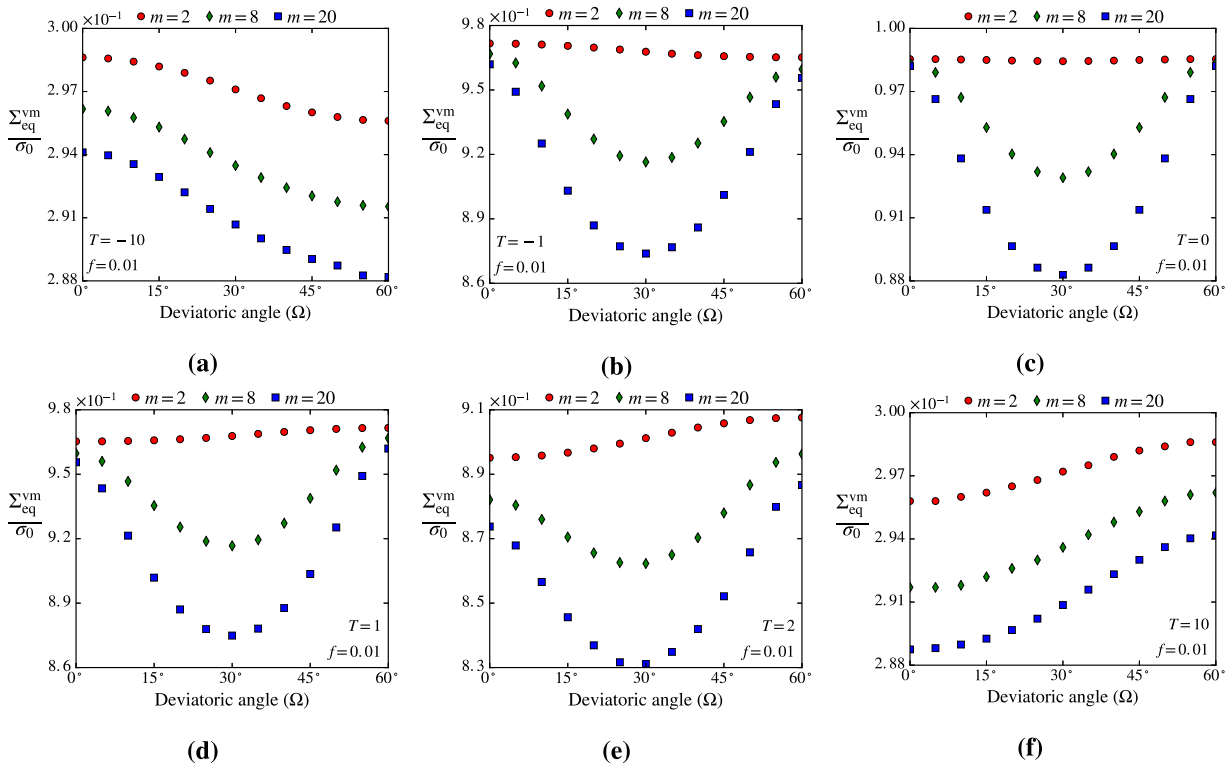

Fig. 7. Yield points in terms of the normalized von Mises equivalent stress ($\Sigma_{eq}^{vm}/\sigma_0$) from the FE analyses of a hollow sphere with porosity $f = 0.01$. The stress triaxiality ratios correspond to (**a**) $T = -10$, (**b**) $T = -1$, (**c**) $T = 0$, (**d**) $T = 1$, (**e**) $T = 2$, and (**f**) $T = 10$. The results for $T = 0$ are similar to the underlying matrix yield surface up to a size reduction factor governed by the porosity (For interpretation of the references to colour in this figure, the reader is referred to the web version of this article.).

In the case of the quadratic matrix yield surface ($m = 2$), the yield strength of the RVE attains a minimum for generalized tension for positive stress triaxiality ratios and increases monotonically with the deviatoric angle towards generalized compression. The opposite trend is found for negative stress triaxiality ratios. Thus, the existence of a material heterogeneity in the form of a void introduces a J_3 dependence in the yield condition for the porous solid even when the matrix yield surface only depends on J_2. Similar results have been reported in numerical studies in the literature (Cazacu et al., 2013; Keralavarma, 2017; Thoré et al., 2011). This J_3 dependence is not predicted by the Gurson model, but can be captured if higher-order terms are included in the series expansion of the microscopic (matrix) dissipation function (Leblond and Morin, 2014) or if the microscopic dissipation is exactly integrated over the spatial domain (Benallal, 2017; 2018; Benallal et al., 2014; Cazacu et al., 2013). However, we should note that the influence of J_3 on the macroscopic yield strength is rather small for the quadratic matrix yield surface ($m = 2$), and is most likely of second-order importance for structural applications, even though it can lead to quite pronounced differences in terms of porosity evolution for large deformations (Alves et al., 2014).

When the matrix material has a non-quadratic yield function ($m = 8$ or $m = 20$), the macroscopic J_3 dependence of the porous solid resembles that of the underlying matrix material for shear-dominated loading states and up to intermediate levels of stress triaxiality (e.g. $|T| \sim 1$). Consequently, the yield strength is minimized around generalized shear ($\Omega = 30^\circ$), which is readily seen from Fig. 7(b)–7(e). We note that the difference in yield strength between generalized compression and tension prevails for non-zero stress triaxiality ratios, but the effect of J_3 associated with the underlying matrix yield surface is more protrusive. However, when the magnitude of the stress triaxiality ratio becomes sufficiently high (e.g. $|T| \sim 10$), we observe similar behaviour that was found for the quadratic matrix yield surface, governed by a monotonic increase or decrease in yield strength with the deviatoric angle depending upon the sign of the hydrostatic stress (or equivalently the stress triaxiality). If we compare the yield strength for opposite stress triaxiality ratios, i.e. $\pm T$, they are related according to $\Sigma_{\text{eq}}^{\text{vm}}(T, \Omega) = \Sigma_{\text{eq}}^{\text{vm}}(-T, 60^\circ - \Omega)$, which is observed from Fig. 7(a) and 7(f) or 7(b) and 7(d). This feature of the macroscopic yield surface entails centro-symmetry, for which the definition may be written as

$$\Phi(\Sigma_{\text{eq}}^{\text{vm}}, \Sigma_{\text{h}}, \Omega) = \Phi(\Sigma_{\text{eq}}^{\text{vm}}, -\Sigma_{\text{h}}, 60^\circ - \Omega) \tag{26}$$

This is a general property for porous plastic materials governed by matrix yield functions that are even functions of the stress state (Cazacu et al., 2019). From Fig. 7(a) and 7(f) it also appears that the difference between the yield strength in generalized tension and generalized compression becomes greater when the exponent m of the matrix yield function increases. It is worthwhile to mention that even though we observe a yield strength difference between generalized tension and generalized compression for the stress triaxiality ratios with highest magnitude ($|T| = 10$), this difference is only $1\% - 2\%$ depending upon the matrix yield surface exponent. Consequently, there is only a slight effect of J_3 on the macroscopic yielding for high stress triaxiality ratios even when the matrix material is governed by a J_3-dependent yield surface.

To shed more light on the appearance of the macroscopic yield surface for non-quadratic matrix yield surfaces, Figs. 8 and 9 show plots of the yield loci obtained from the FE unit cell analyses for $m = 8$ and $m = 20$, respectively. The depicted yield loci correspond to level curves (contours) of constant macroscopic stress triaxiality projected onto the deviatoric plane. Hence, the data points on a yield locus are generally not lying on the same deviatoric plane in the principal stress space (Keralavarma, 2017). We note that only yield points for $\Omega = 0^\circ, 5^\circ, \ldots 60^\circ$ were evaluated and these points were subsequently mirrored to map up the entire yield locus, utilizing the isotropy of the porous plastic solid. The results presented in these figures correspond to the three different porosity levels used in the FE analyses and are labelled as follows: $f = 0.1$ (solid blue lines with circle markers), $f = 0.01$ (dotted red lines with square markers), and $f = 0.001$ (dashed black lines with diamond markers). Figs. 8(a)–8(i) and 9(a)–9(i) pertain to increasing values of the macroscopic stress triaxiality ratio: $T = -10, -2, -1, 0, 0.25, 0.5, 1, 2, 10$.

When the magnitude of the macroscopic stress triaxiality is close to zero (see Figs. 8(d)–8(f) and 9(d)–9(f)), the yield loci are very similar in shape to the underlying matrix yield surface, which is retained for a macroscopic stress triaxiality ratio of $T = 0$. This is readily seen from Figs. 8(d) and 9(d). Thus, in the case of pure shear stress states, the yield surface of the porous ductile solid coincides with the yield surface of the matrix material, except for a yield domain size reduction dictated by the porosity level. When the magnitude of the stress triaxiality ratio increases to $|T| = 1$ and 2 (see Figs. 8(b), 8(c), 8(g), 8(h), 9(b), 9(c), 9(g) and 9(h)), the highest porosity level ($f = 0.1$) clearly results in a more rounded triangular shape, while the two lower porosity levels ($f = 0.01, 0.001$) still display sharper corners. Thus, for rather high but realistic stress triaxiality levels that are frequently encountered in numerical simulations of structural components, the effect of J_3 on the macroscopic yielding of a porous ductile solid is greatly influenced by the porosity level. By increasing the magnitude of the stress triaxiality even further (e.g. $T = \pm 10$), we readily see from Figs. 8(a), 8(i), 9(a) and 9(i) that the macroscopic yield loci appear almost circular regardless of the curvature of the underlying matrix yield surface (i.e. the value of m). This observation pertains to all three porosity levels and implies that under predominant macroscopic hydrostatic loading, either with positive or negative stress triaxiality, the macroscopic yielding is almost unaffected by the deviatoric loading condition. However, we should keep in mind that Fig. 7(a) and 7(f) revealed a slight difference in the yield strength between generalized tension and compression for the highest stress triaxiality magnitudes, but this effect is so small that it is hardly visible on the yield loci depicted in Figs. 8(a), 8(i), 9(a) and 9(i). Moreover, in the hydrostatic limit (i.e. $\Sigma_{\text{eq}}^{\text{vm}} = 0$) the yield locus coalesces to a single point in the deviatoric plane; thus, it seems only natural that the yield loci for close-to-hydrostatic stress states (i.e. $\Sigma_{\text{eq}}^{\text{vm}} \approx 0$ and $|T| \gg 1$) become nearly circular.

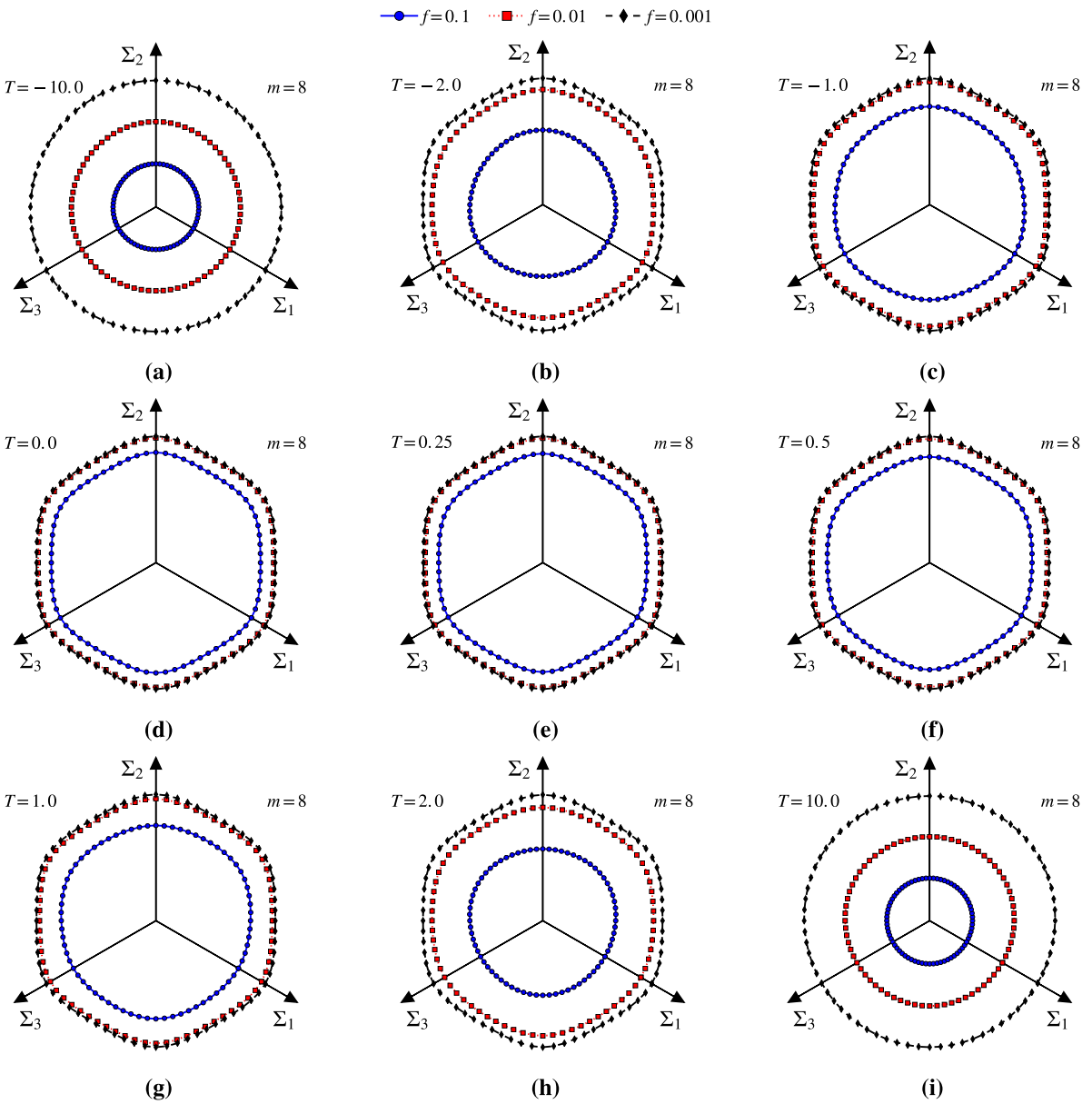

Fig. 8. Discrete yield loci in the principal stress space for $m = 8$ and constant stress triaxiality ratios projected onto the deviatoric plane. All three porosity levels employed in this work are shown; $f = 0.1$ (blue solid lines - circle markers), $f = 0.01$ (red dotted lines - square markers), and $f = 0.001$ (black dashed lines - diamond markers). (For interpretation of the references to colour in this figure legend, the reader is referred to the web version of this article.)

From the results presented in Figs. 8 and 9, we conclude that the porosity level plays a key role in how quickly the macroscopic yield surface evolves from the hexagonal shape that is reminiscent of the matrix yield surface (see Fig. 2), to the rounded triangular shape, and finally to the nearly circular shape prevalent for predominant hydrostatic stress states. A similar finding was reported in the previous study by Revil-Baudard and Cazacu (2014a) for a Tresca matrix behaviour, which shares many of the same features as the matrix yield surface with $m = 20$ used in this study. We note that there are rather small differences between the macroscopic yield points for $f = 0.01$ and $f = 0.001$ up to rather high stress triaxiality ratios. Roughly speaking, we observe almost no difference between yield loci for $f = 0.001$ and $f = 0.01$ within a range of stress triaxiality ratios corresponding to $-1 \leq T \leq 1$ (see Figs. 8(c)–8(g) and 9(c)–9(g)). This is actually quite an important range of stress triaxiality ratios and porosity levels in terms of practical applications for structural metal alloys. The effect of the porosity becomes greater when the magnitude of the stress triaxiality ratio increases. From the numerical results shown in Figs. 8 and 9, we observe pronounced differences between the yield loci for all three porosity levels when the magnitude of the stress triaxiality ratio is larger than roughly $|T| \approx 2$. In the case of the highest magnitude of the stress triaxiality ratio ($|T| = 10$), the yield limits are very different depending upon the porosity level. As such, the hydrostatic limit

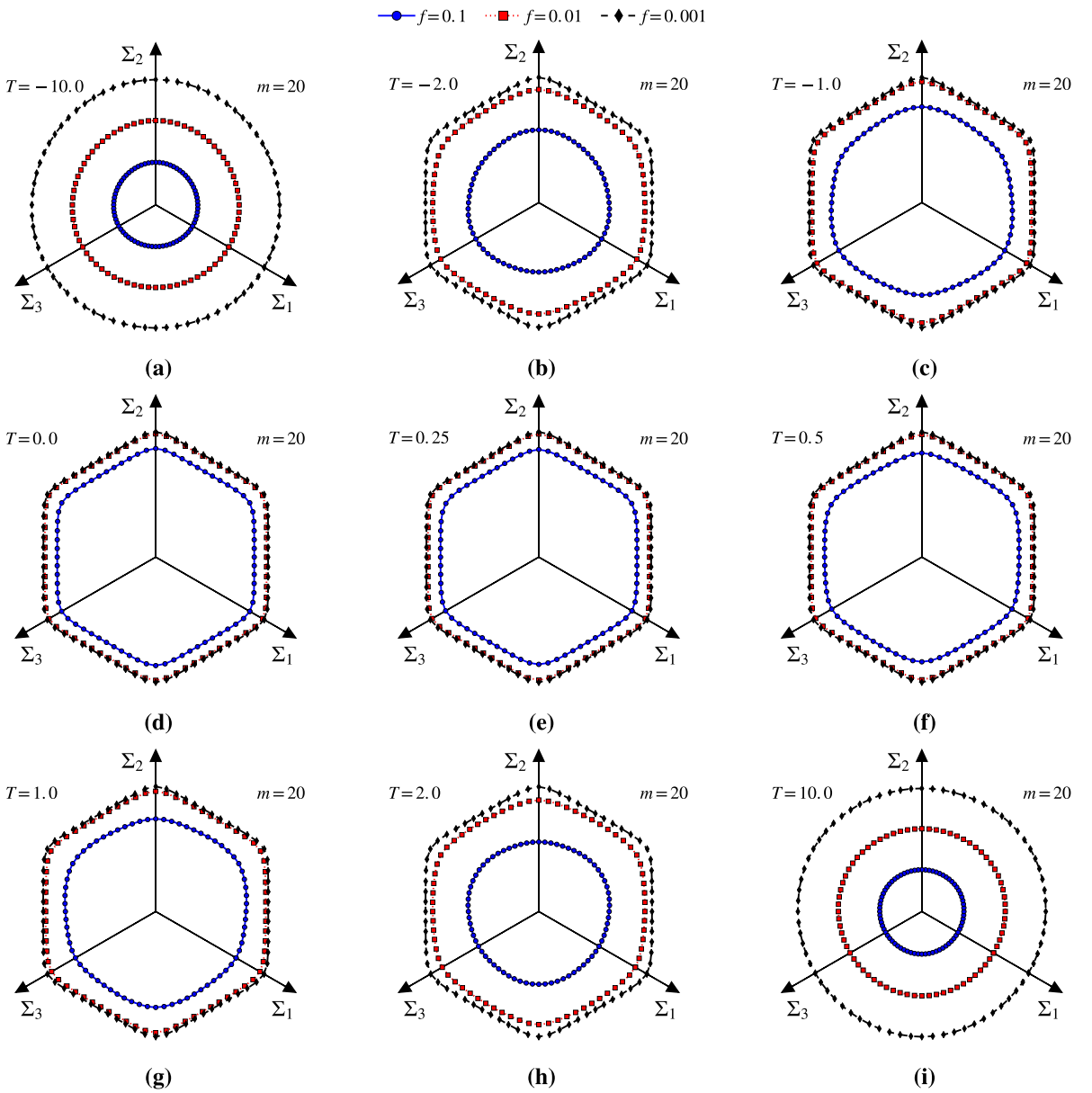

Fig. 9. Discrete yield loci in the principal stress space for $m = 20$ and constant stress triaxiality ratios projected onto the deviatoric plane. All three porosity levels employed in this work are shown; $f = 0.1$ (blue solid lines - circle markers), $f = 0.01$ (red dotted lines - square markers), and $f = 0.001$ (black dashed lines - diamond markers). (For interpretation of the references to colour in this figure legend, the reader is referred to the web version of this article.)

(i.e. $\Sigma_{\text{eq}}^{\text{vm}} = 0$) is greatly affected by the porosity level, which is in accordance to the porous plasticity models presented in Section 4.

We also find that the yield locus shape transition is influenced by the magnitude of the yield surface exponent (m). This is to some extent observed by comparing the yield loci in e.g. Figs. 8(g) and 9(g). However, the influence of the matrix yield surface exponent on the shape transition seems to be only second order to that of the porosity level, and the porosity is clearly the dominant factor for the yield surface evolution with increasing magnitude of the stress triaxiality. This was also addressed in the study by Revil-Baudard and Cazacu (2014a) showing 3D yield surfaces for constant levels of the mean strain.

Before we proceed to the assessment of the two porous plasticity models, we would like to highlight a particular observation from the numerical analyses with the quadratic matrix yield function ($m = 2$). When $T = 0$, the porous plasticity models display a yield surface that is identical to the underlying matrix, except that the yield strength is reduced by a factor that scales with the porosity level. With reference to Fig. 7(c), this suggests that we should obtain a straight line for $m = 2$. However, from the numerical results shown in Fig. 10, we may notice that we do not obtain *exactly* a straight line, although

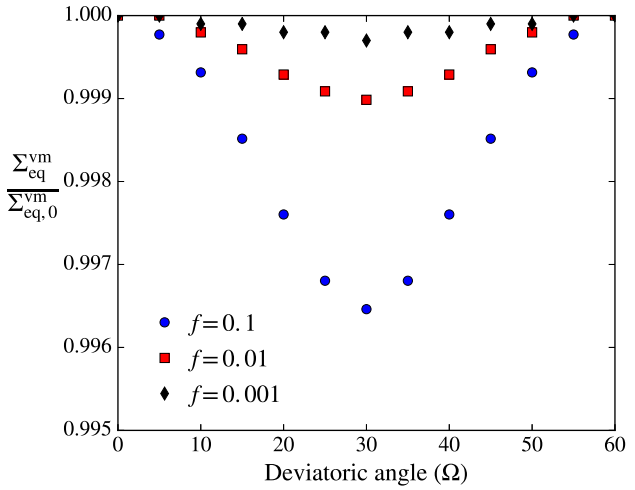

Fig. 10. Yield points for $m = 2$ and $T = 0$ plotted against the macroscopic deviatoric angle. The data points correspond to the von Mises equivalent stress at yielding (Σ^{vm}_{eq}) normalized by the von Mises equivalent stress at yielding in generalized tension ($\Sigma^{vm}_{eq,0} = \Sigma^{vm}_{eq}(\Omega = 0^\circ)$) for all three levels of porosity.

the deviation is only slight. The yield strength rather decreases for generalized shear and monotonically increases towards the axisymmetric limits. The observed effect is consistent and pertains to all three levels of porosity, but it decreases with decreasing porosity. As such, we do not believe this to be caused by numerical errors, but rather to result from the spatial heterogeneity of the mechanical fields and that the numerical analyses accommodate a more general set of velocity fields compared to the unique trial velocity field used in the upper-bound limit analysis.

6.2. Assessment of the porous plasticity models

In this section, we compare the two analytical models presented in Sections 4.1 and 4.2 to the numerical data obtained from the FE limit analyses and discuss their respective performance in light of the yield limits provided by the FE calculations. The latter are considered to be the exact yield limits for the hollow sphere model, while the two analytical models are upper-bound solutions. However, only the model developed by Benallal (2017, 2018) can be *a priori* considered as a rigorous upper-bound solution (see Section 4.1), since the heuristic extension is only mathematically rigorous for the quadratic matrix yield surface; i.e. when it reduces to the original Gurson model (Gurson, 1977).

Figs. 11–13 compare yield loci for the porous plasticity models to the FE limit analyses for all three matrix yield surface shapes and for all porosity levels examined herein. The solid and dashed lines correspond to the rigorous model and the heuristic model, respectively, while the circle markers indicate the FE yield points. The porosity levels are indicated by different colours: $f = 0.001$ (green), $f = 0.01$ (red), and $f = 0.1$ (blue). We must emphasize that the yield loci represent contours of constant stress triaxiality and not levels of constant hydrostatic stress. As such, the yield loci are curved sections of the yield surface in the principal stress space and the loci derived from the FE analyses, the rigorous model, and the heuristic model generally do not lie in the same plane. However, they correspond to sections of the same macroscopic stress triaxiality, which is an important parameter that is frequently used as a reference parameter in FE simulations of material tests and structural components and is of key importance for the porosity evolution in large-strain theory.

From Figs. 11–13, we observe that the results obtained with the rigorous model are in good agreement to those of the FE simulations for all stress states and shapes of the matrix yield surface. The predictions are less accurate for high porosity levels, which conforms with the results of the previous study by Cazacu et al. (2014b), but the shape of the yield loci are still in very good agreement to the FE simulations. We observe that the rigorous model reflects the transformation of the yield surface with stress triaxiality, from the hexagonal shape ($\pi/6$-symmetry) at low stress triaxiality to the rounded triangular shape ($\pi/3$-symmetry) at fairly high stress triaxiality. This is perhaps most easily verified from Fig. 13. Both the rigorous model and the heuristic model indeed provide upper-bound solutions for the matrix yield surfaces and porosity levels studied herein. This is *a priori* satisfied for the rigorous model due to the exact solution of the kinematic limit analysis, but cannot be guaranteed for the heuristic model other than for $m = 2$.

While the rigorous model generally provides rather accurate predictions, we observe that also the heuristic model predicts the yield stress with good accuracy for all stress states and shapes of the matrix yield surface when the porosity is low ($f = 0.001$). Even for the intermediate porosity level ($f = 0.01$) the predictions of the heuristic model are rather similar to those of the rigorous model and the FE results, although some minor discrepancies are visible, especially for stress states close to generalized tension or generalized compression (see e.g. Figs. 12(e) and 13(e)). When the porosity is very high (i.e. $f = 0.1$), the accuracy of the heuristic model deteriorates for the non-quadratic matrix yield surfaces. The largest discrepancy is observed around axisymmetric stress states ($\Omega = 0^\circ$ or 60°) and intermediate to high stress triaxiality ratios ($|T| \approx 1 - 2$

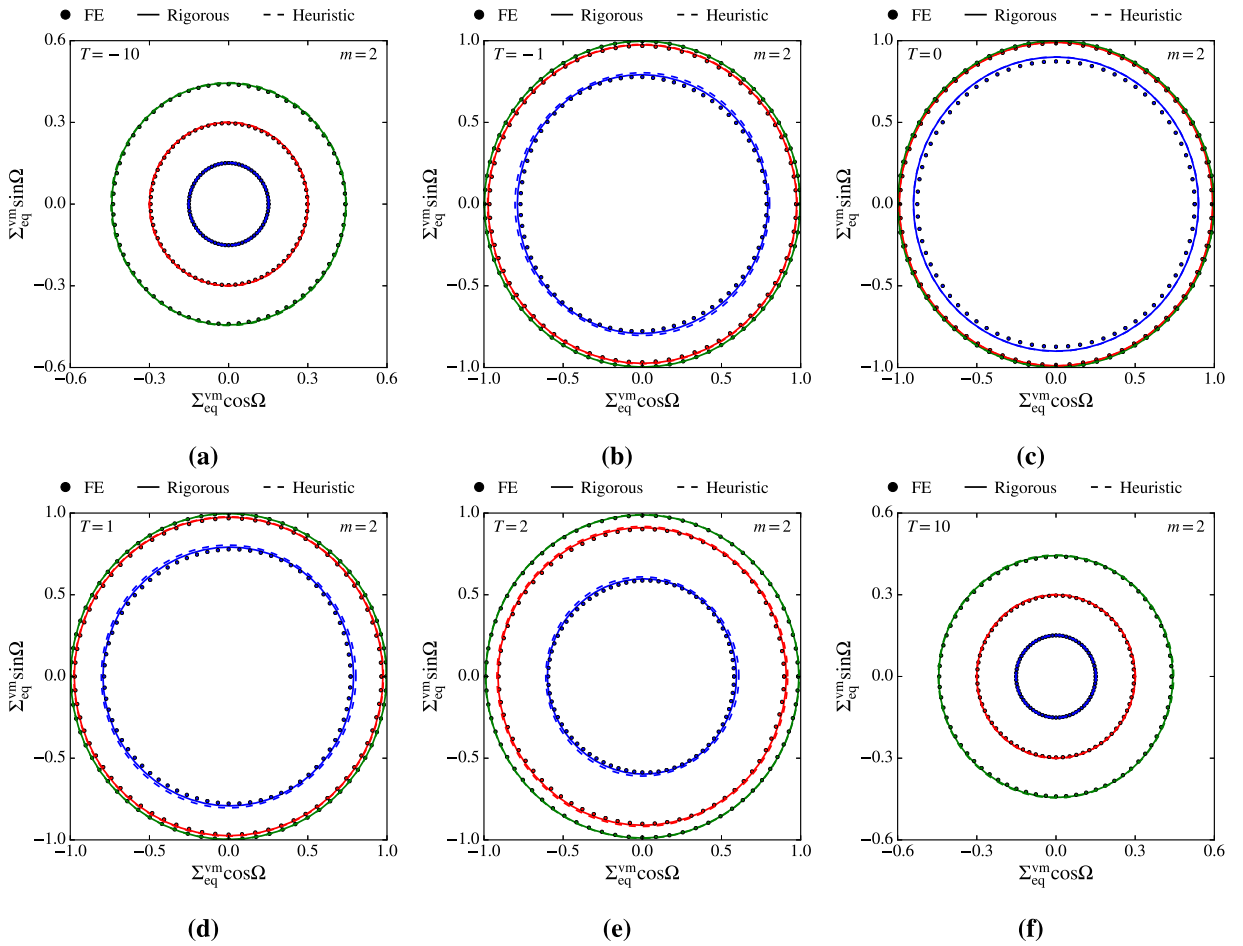

Fig. 11. Comparison between the unit cell results (solid points), the rigorous model (solid lines), and the heuristic model (dashed lines) for yield surface exponent $m = 2$. The plots correspond to porosity levels $f = 0.001$ (green curves), $f = 0.01$ (red curves), and $f = 0.1$ (blue curves) and stress triaxiality levels of (a) $T = -10$, (b) $T = -1$, (c) $T = 0$, (d) $T = 1$, (e) $T = 2$, (f) $T = 10$. (For interpretation of the references to colour in this figure legend, the reader is referred to the web version of this article.)

in these analyses), where the heuristic model markedly overestimates the actual yield strength evaluated from the FE calculations. The main reason for these deviations is that the heuristic model predicts a macroscopic yield surface that retains the shape of the underlying matrix yield surface regardless of the stress triaxiality ratio and the porosity level. Consequently, the heuristic model cannot account for the transformation of the macroscopic yield surface that drastically changes the shape of the yield loci; i.e. from the hexagonal shape to the rounded triangular shape for increasing triaxiality. This is neither in accordance to the predictions obtained in the FE limit analyses nor to the predictions of the rigorous porous plasticity model, which both display this type of yield surface transformation. Since this transformation was found to be closely related to the porosity level (see e.g. Fig. 9(g) and the discussion in Section 6.1), where a high porosity level facilitates earlier development of the rounded triangular shape, the predictions of the heuristic model are consequently hampered by increasing porosity level. However, when the magnitude of the stress triaxiality becomes sufficiently high (e.g. $|T| \sim 10$ in our results), the predictions of the heuristic model is seen to agree well with both the FE yield points and the predictions of the rigorous model. Whether this is of practical relevance is of course debatable, since such high stress triaxiality ratios are rarely encountered in structural applications due to blunting of the highly constrained regions during deformation.

Figs. 11–13 provide a reasonable comparison of the porous plasticity models to the FE data and clearly highlight the predictive capabilities of the two models. However, the quality of the predictions is perhaps more easily assessed from Figs. 14 and 15, which show how the yield stress in terms of normalized von Mises equivalent stress ($\Sigma_{eq}^{vm}/\sigma_0$) varies with the macroscopic deviatoric angle (Ω).

Fig. 14(a)–14(f) pertain to all three matrix yield surface shapes at different levels of stress triaxiality. The solid lines correspond to the rigorous model, the dashed lines to the heuristic model and the points indicated by markers pertain to the FE yield points. The different matrix yield surface shapes are labelled as follows: (i) $m = 2$ is highlighted with red colour and solid markers, (ii) $m = 8$ is highlighted with green colour and diamond markers, while (iii) $m = 20$ is highlighted with

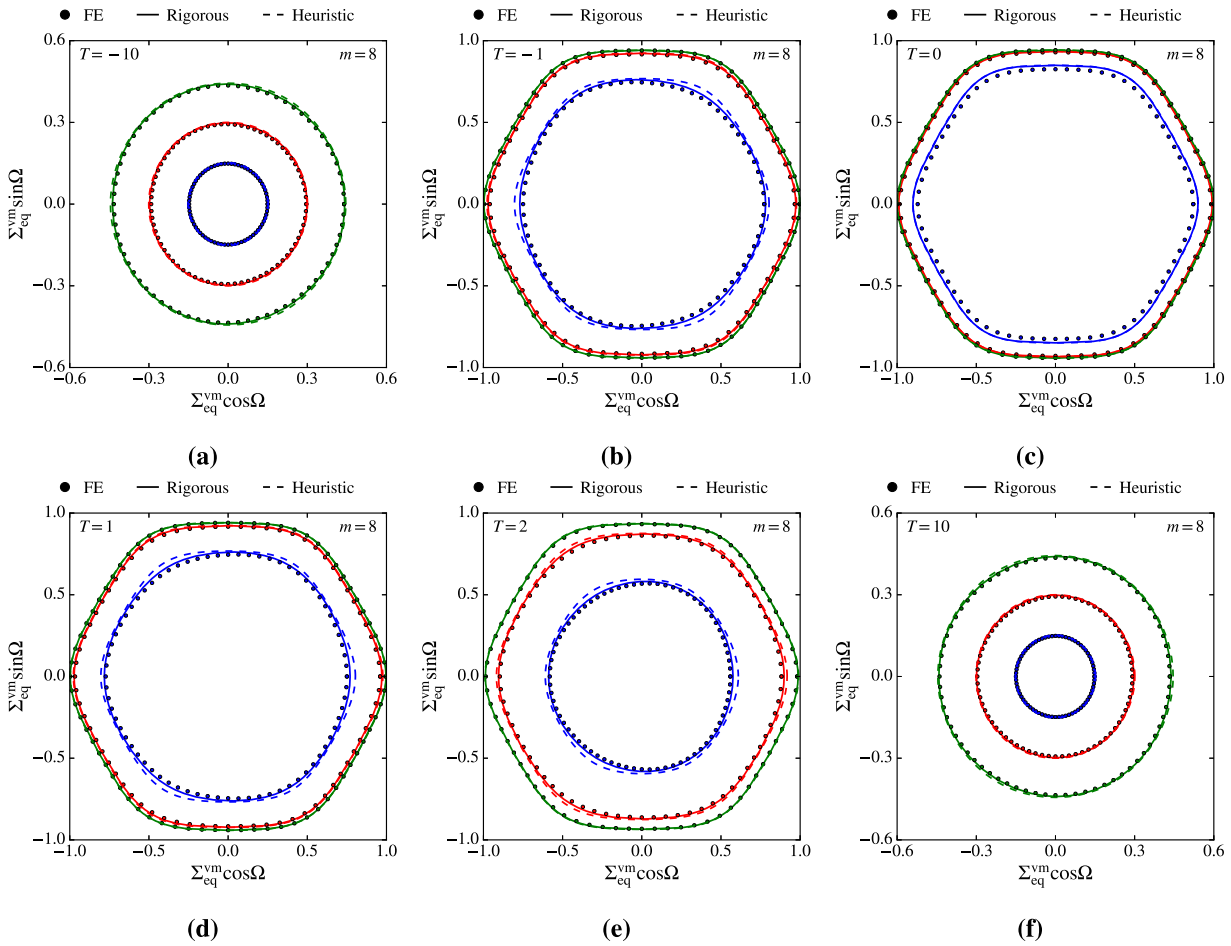

Fig. 12. Comparison between the unit cell results (solid points), the rigorous model (solid lines), and the heuristic model (dashed lines) for yield surface exponent $m = 8$. The plots correspond to porosity levels $f = 0.001$ (green curves), $f = 0.01$ (red curves), and $f = 0.1$ (blue curves) and stress triaxiality levels of (a) $T = -10$, (b) $T = -1$, (c) $T = 0$, (d) $T = 1$, (e) $T = 2$, (f) $T = 10$. (For interpretation of the references to colour in this figure legend, the reader is referred to the web version of this article.)

blue colour and square markers. The results pertain to the intermediate porosity level $f = 0.01$ and the following stress triaxiality ratios; (**a**) $T = -10$, (**b**) $T = -1$, (**c**) $T = 0$, (**d**) $T = 1$, (**e**) $T = 2$, and (**f**) $T = 10$.

We readily observe that the rigorous model is capable of describing the evolution of the yield surface from the hexagonal shape at low stress triaxialities to the rounded circular shape for higher stress triaxialities. The heuristic model fails to do so because it retains the shape of the Hershey-Hosford yield surface for any constant hydrostatic stress level, which gives the same yield stress in generalized tension and compression. Moreover, the rigorous model reflects the centro-symmetry of the macroscopic yield surface, which can be verified by comparing Fig. 14(a) and 14(f) or 14(b) and 14(d), respectively. We note that the rigorous model generally provides more accurate predictions of the yield stress compared to the heuristic counterpart, especially in regions close to generalized axisymmetric loading. However, for stress states around generalized shear ($\Omega = 30^\circ$) the heuristic model is actually in closer agreement with the FE results. Moreover, Fig. 14(b)–14(d) show that the model predictions are generally better for generalized shear states than for stress states closer to generalized compression or tension when the magnitude of the stress triaxiality is low or intermediate. When the magnitude of the stress triaxiality increases, the porous plasticity models give enhanced predictions in either generalized tension (negative T) or generalized compression (positive T). This is observed in Fig. 14(a) and 14(f) and demonstrates that the yield surface evolution with T is not sufficiently rapid for the rigorous model.

Fig. 15(a)–15(f) compare the two porous plasticity models with the FE results for $m = 8$ at the three different porosity levels: (i) $f = 0.1$ (red lines and circle markers), (ii) $f = 0.01$ (blue lines and diamond markers), and (iii) $f = 0.001$ (green lines and square markers). These figures demonstrate that for a given matrix yield surface, increasing the porosity generally deteriorates the predictions of the heuristic model. The rigorous model and the FE data display strong effects of the deviatoric angle for large porosity levels, leading to large differences between the yield stress in generalized tension and compression, which the heuristic model cannot describe. However, when the stress triaxiality magnitude becomes sufficiently high (e.g. $|T| \approx 10$), the two porous plasticity models are both in very good agreement to the FE limit analyses. If the

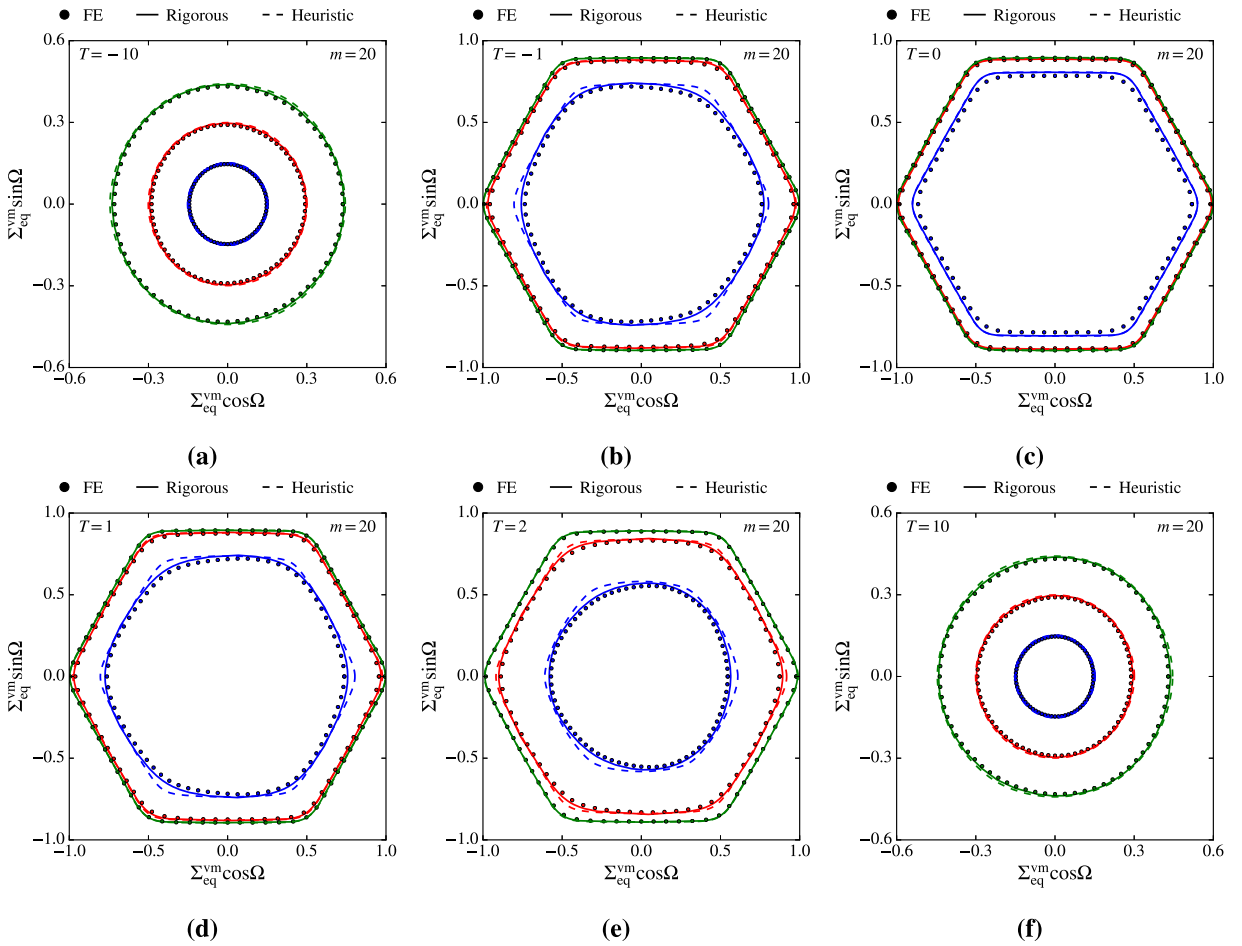

Fig. 13. Comparison between the unit cell results (solid points), the rigorous model (solid lines), and the heuristic model (dashed lines) for yield surface exponent $m = 20$. The plots correspond to porosity levels $f = 0.001$ (green curves), $f = 0.01$ (red curves), and $f = 0.1$ (blue curves) and stress triaxiality levels of (a) $T = -10$, (b) $T = -1$, (c) $T = 0$, (d) $T = 1$, (e) $T = 2$, (f) $T = 10$. (For interpretation of the references to colour in this figure legend, the reader is referred to the web version of this article.)

porosity level is fairly low (e.g. $f = 0.001$), the two models are more or less coincident and both fit very well with the FE results. The intermediate porosity level ($f = 0.01$) also gives reasonably good correspondence between the two porous plasticity models. However, we note that for intermediate and high stress triaxiality magnitudes (e.g. $|T| = 1, 2$) and deviatoric angles close to $\Omega = 0^\circ$ and $\Omega = 60^\circ$, the predictions of the heuristic model are higher than the rigorous model and less accurate compared to the FE limit analyses. This was also seen from Figs. 12 and 13.

While there clearly is an inherent limitation to the predictive capabilities of the heuristic porous plasticity model, we infer from these results that for (i) low, but realistic, porosity levels, (ii) low stress triaxiality ratios, and (iii) very high stress triaxiality ratios, the predictions of the heuristic model are in good agreement with those of the rigorous model and the FE limit analyses. Our preliminary conclusion is that the heuristic model demonstrates sufficient predictive capabilities to merit use in numerical analyses of structural components made from metal alloys, where the intrinsic porosity or volume fraction of void-nucleating particles is typically much lower than $f = 0.1$.

The comparison between the porous plasticity models and the FE results have so far been based on data for constant levels of stress triaxiality. Some caution should then be exercised because the yield points are extracted from curved yield surface sections that are projected onto the deviatoric plane. Consequently, these data points generally correspond to different levels of hydrostatic stress. To aid the interpretation and to corroborate the discussion regarding the performance of the two porous plasticity models, Figs. 16(a)–16(c), 17(a)–17(c), 18(a)–18(c) show yield loci in the meridian plane for (**a**) $\Omega = 0^\circ$, (**b**), $\Omega = 30^\circ$, and (**c**) $\Omega = 60^\circ$. This allows to assess the performance of the two porous plasticity models for constant hydrostatic stress levels. The figures correspond to $m = 2$, 8, and 20, respectively. Yield points from the FE limit analyses are indicated by the circle markers, the predictions of the rigorous model are indicated by the solid lines, and the predictions of the heuristic model are indicated by the dashed lines. All three porosity levels used in this study are shown in the figures to highlight the effect of porosity.

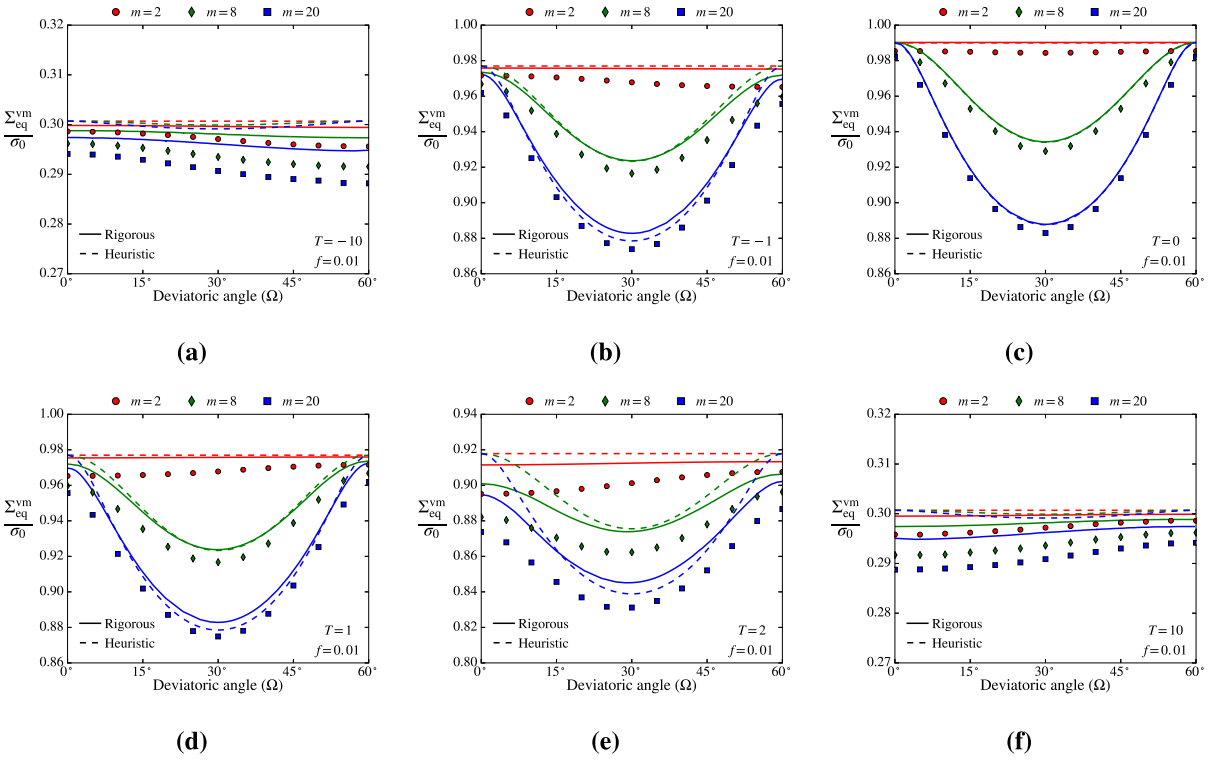

Fig. 14. Yield points in terms of the normalized von Mises equivalent stress ($\Sigma_{eq}^{vm}/\sigma_0$) plotted against the deviatoric angle (Ω) for the intermediate porosity $f = 0.01$. Results are shown for the rigorous model (solid lines), the heuristic model (dashed lines), and the FE limit analyses (markers) in the case of $m = 2$ (red lines and circle markers), $m = 8$ (green lines and diamond markers), and $m = 20$ (blue lines and square markers). The stress triaxiality ratios correspond to (**a**) $T = -10$, (**b**) $T = -1$, (**c**) $T = 0$, (**d**) $T = 1$, (**e**) $T = 2$, and (**f**) $T = 10$. (For interpretation of the references to colour in this figure legend, the reader is referred to the web version of this article.)

The curves plotted in Fig. 16 show that in the case of the quadratic matrix yield surface, the predictions are rather accurate for both porous plasticity models regardless of the stress triaxiality ratio. However, we observe slight deviations from the FE limit analyses for both porous plasticity models as the porosity level increases. This can be seen from the yield loci that correspond to the highest porosity level $f = 0.1$. Perhaps most apparent is the difference for purely deviatoric loading (i.e. $\Sigma_h = 0$), where the two porous plasticity models give identical predictions and provide too high estimates for macroscopic yielding. This is a relatively well-known issue and can be remedied in both porous plasticity models by e.g. introducing the q_i parameters suggested by Tvergaard (1981); however, at the expense of violating the exact representation of the hydrostatic limit. Even in the case of the quadratic matrix yield function, we observe differences between the two porous plasticity models that are apparent for all three deviatoric angles shown in the figures (i.e. $\Omega = 0^\circ, 30^\circ, 60^\circ$). The rigorous model is seen to provide a slightly tighter upper-bound estimate for the quadratic matrix, which can be explained by the dependence of the parameters *a, R, P* and *Q* in the yield function given by Eq. (16) on the macroscopic stress triaxiality *T*. This was also shown in Fig. 3 and to some extent discussed in Section 4.3. These small discrepancies set aside, the predictions of the porous plasticity models should be considered rather accurate for all stress states and porosity levels when the matrix material is governed by the quadratic yield function. This very good agreement between the porous plasticity models and the FE limit analyses for $m = 2$ is not surprising since this corresponds to the original Gurson model (heuristic), which has found widespread use in the literature, and a Gurson-type model with an exact integration of the microscopic plastic dissipation function over the spatial RVE domain (rigorous).

When the matrix material is governed by a non-quadratic yield function, see Figs. 17 and 18, the differences between the porous plasticity models are more pronounced. As noted in Section 4.3, the rigorous model usually provides a tighter upper-bound solution compared to the heuristic model. The exceptions pertain to stress states close to generalized shear ($\Omega = 30^\circ$), as seen from Fig. 18(b), where the rigorous model gives slightly higher values for the equivalent stress at yielding for some stress triaxiality ratios. This was also observed in Fig. 14(b), 14(d) and 14(e). However, we must emphasize that this difference is very small and the rigorous model usually gives improved conformity to the FE limit analyses. The most marked differences between the two porous plasticity models are observed for stress states corresponding to generalized tension or generalized compression (see Figs. 17(a), 17(c), 18(a), and 18(c)), especially for intermediate and up to rather high stress triaxiality ratios. While the axisymmetric stress states ($\Omega = 0^\circ$ and $\Omega = 60^\circ$) are not well reflected by the heuristic model, at least for rather high porosity levels, the stress states corresponding to generalized shear ($\Omega = 30^\circ$) are accurately predicted

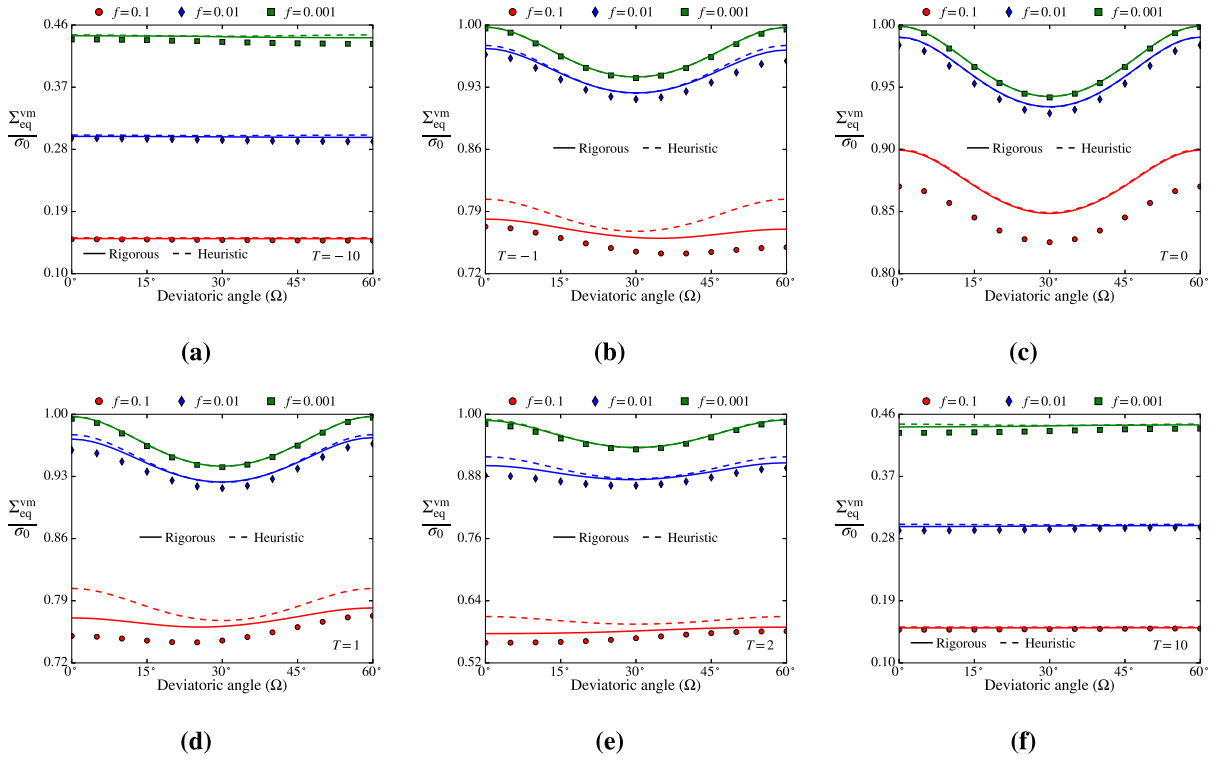

Fig. 15. Yield points in terms of the normalized von Mises equivalent stress ($\Sigma_{eq}^{vm}/\sigma_0$) plotted against the deviatoric angle (Ω) for the matrix yield surface with $m = 8$. Results are shown for the rigorous model (solid lines), the heuristic model (dashed lines), and the FE limit analyses (markers) in the case of $f = 0.1$ (red lines and circle markers), $f = 0.01$ (blue lines and diamond markers), and $f = 0.001$ (green lines and square markers). The stress triaxiality ratios correspond to (**a**) $T = -10$, (**b**) $T = -1$, (**c**) $T = 0$, (**d**) $T = 1$, (**e**) $T = 2$, and (**f**) $T = 10$. (For interpretation of the references to colour in this figure legend, the reader is referred to the web version of this article.)

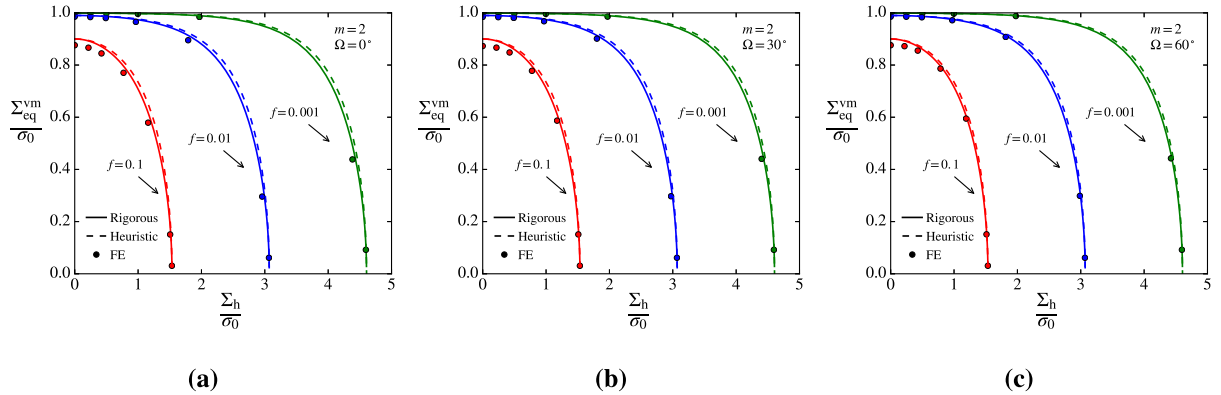

Fig. 16. Yield points plotted in the meridian plane for yield surface exponent $m = 2$. The data correspond to the porosity levels $f = 0.001$ (green), $f = 0.01$ (blue), and $f = 0.1$ (red). FE yield points are indicated by the circle markers. (For interpretation of the references to colour in this figure legend, the reader is referred to the web version of this article.)

by both porous plasticity models. From Figs. 17(b) and 18(b) we see that there are only small differences between the two porous plasticity models, and they both conform well to the FE limit analyses. This observation applies to all porosity levels.

As the stress triaxiality ratio becomes sufficiently high, i.e. approaching the hydrostatic limit, we infer from Figs. 16–18 that both porous plasticity models yield very accurate predictions. Based on the stress states imposed in the FE limit analyses herein, we find that the predictions are very good when $T = 10$ and $T = 50$. Indeed, in the hydrostatic limit (i.e. $\Sigma_{eq}^{vm} = 0$), the two models conform and give the same yield limit, viz.

$$|\Sigma_h| = -\frac{2}{3}\ln(f)\sigma_0 \tag{27}$$

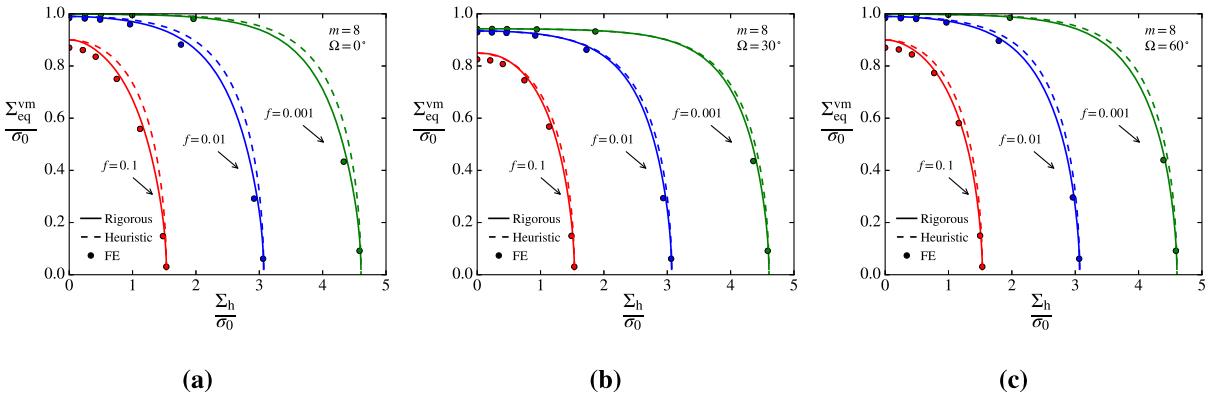

Fig. 17. Yield points plotted in the meridian plane for yield surface exponent $m = 8$. The data correspond to the porosity levels $f = 0.001$ (green), $f = 0.01$ (blue), and $f = 0.1$ (red). FE yield points are indicated by the circle markers. (For interpretation of the references to colour in this figure legend, the reader is referred to the web version of this article.)

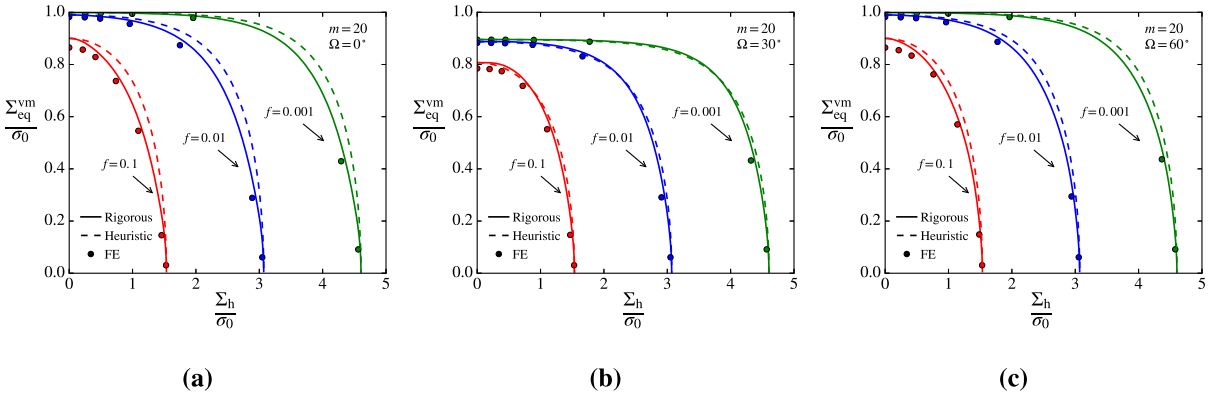

Fig. 18. Yield points plotted in the meridian plane for yield surface exponent $m = 20$. The data correspond to the porosity levels $f = 0.001$ (green), $f = 0.01$ (blue), and $f = 0.1$ (red). FE yield points are indicated by the circle markers. (For interpretation of the references to colour in this figure legend, the reader is referred to the web version of this article.)

In this case, the porous plasticity models give the exact yield limit for the hollow sphere RVE, since the trial velocity field corresponds to the exact velocity field for an entirely hydrostatic loading. This was also demonstrated in the study by Yi and Wang (1989) in which the lower-bound and upper-bound limit analyses coincide in the hydrostatic limit. Thus, the predictions of the porous plasticity models are expected to match perfectly for $T \to \pm\infty$. Even though this is not explicitly investigated in the current work, since the maximum applied triaxiality is $T = 50$, results from FE limit analyses presented by Guo et al. (2008) show that the FE results and the Gurson yield surface coincide in the hydrostatic limit (see Figs. 4 and 5 in the referenced paper). A similar result has been attained for a Tresca matrix material (Cazacu et al., 2014a).

The two porous plasticity models also coincide for purely deviatoric loading (i.e. $\Sigma_h = 0$), where both models reduce to the underlying Hershey-Hosford yield function scaled down by a size reduction factor, according to

$$\Sigma_{eq} = (1 - f)\sigma_0 \tag{28}$$

However, for purely deviatoric loading states, the porous plasticity models give too high estimates of the yield strength and do not represent the exact limit. In this case, the trial velocity field used in the upper-bound limit analysis does not correspond to the exact velocity field. Although this holds true regardless of the macroscopic deviatoric angle (Ω), we note that the overestimation of the yield strength is somewhat less for generalized shear states, which is seen from Fig. 14(c) or by comparing e.g. Fig. 18(a)–18(c). Also, the discrepancy seems more pronounced for the highest porosity value, which suggests that the predictions of the porous plasticity models become less accurate with increasing porosity level. This is in agreement to findings reported in the studies by Fritzen et al. (2012) and Cazacu et al. (2014b). A potential way to overcome this issue was proposed by Fritzen et al. (2012), in which the Tvergaard parameters q_i are taken as functions of the porosity f.

While the rigorous model generally provides more accurate results than the heuristic model, which is especially apparent for axisymmetric stress state ($\Omega = 0^\circ$ and $\Omega = 60^\circ$), this drawback is somewhat compensated by the explicit formulation of the heuristic model that makes it simpler for numerical implementation. The implementation of the heuristic model into an FE code (e.g. using UMAT or VUMAT in Abaqus) is rather straightforward and almost identical to the implementation

of the original Gurson model. Moreover, the differences between the heuristic porous plasticity model and the rigorous porous plasticity model are quite small for the lower porosity levels ($f = 0.001, 0.01$), which are also the most realistic porosity levels for many structural metal alloys. The differences between the porous plasticity models are also smaller for lower stress triaxiality ratios, and in the case of $f = 0.01$ the difference is not substantial before the stress triaxiality ratio is between $T = 1$ and $T = 2$. For many structural applications, this is already a very high stress triaxiality level, which also serves as a justification for using the heuristic model in structural analyses. However, we should keep in mind that the porosity evolution can be rather different for large deformations (Cazacu et al., 2014a; Revil-Baudard and Cazacu, 2014b), which affects subsequent yielding and may lead to significant discrepancies as the deformations in structural problems usually involve accumulation of large plastic strains.

Some final remarks in this section are directed towards the effects of large deformations, which have not been addressed in this study. Even though the two porous plasticity models are in quite good agreement to one another, and also to the FE calculations, for many stress states and different porosity levels, this does not necessarily entail that their predictions will be as close or as similar to unit cell calculations when large deformations are taken into account. There are several aspects to this. First, the void shape will clearly evolve as large deformations are accounted for; an effect that is widely reported in the literature (see e.g. Budiansky et al., 1982; Dæhli et al., 2018; Koplik and Needleman, 1988; Nielsen et al., 2012; Pardoen and Hutchinson, 2000; Søvik and Thaulow, 1997). Second, small variations of the yield surface between the two porous plasticity models can lead to rather large discrepancies in the porosity evolution, which is classically updated according to

$$\dot{f} = (1 - f)\mathrm{tr}\mathbf{D}^{\mathrm{p}} \tag{29}$$

where $\mathbf{D}^{\mathrm{p}}$ is the plastic rate-of-deformation tensor. This effect has been studied in some detail for a Mises matrix by Leblond and Morin (2014), where they consider different truncations of the microscopic plastic dissipation series approximation and the corresponding influence on the porosity rate. Further, Alves et al. (2014) compared the porosity evolution of the Gurson model and a Gurson-type porous plasticity model where the microscopic dissipation is exactly integrated over the spatial domain for axisymmetric stress states (Cazacu et al., 2013). Their results show that there are rather pronounced differences between the two porous plasticity models under large deformations, both for positive and negative stress triaxiality levels, and that the model based on the exact integration is in closer agreement with large-deformation unit cell calculations. A similar comparison was made by Cazacu et al. (2014a) between a porous plasticity model for a Tresca-type matrix (Cazacu et al., 2014b) and the original Gurson model in the case of axisymmetric loading. Further, the J_3 dependence of the macroscopic yield surface generally leads to different void evolution in generalized tension and generalized compression. This manifests itself opposite in positive and negative hydrostatic tension, void growth and void collapse, respectively, due to centro-symmetry of the macroscopic yield surface (Alves et al., 2014). Third, predominant deviatoric loading ($T \approx 0$) usually changes the fracture mode from void growth and coalescence to a shear-driven type of fracture. This type of ductile failure is not reflected by the Gurson-type of porous plasticity models discussed herein and would require a suitable void coalescence criterion and preferably also a more advanced porous plasticity model accounting for more general void shapes, such as the model proposed by Madou and Leblond (2012). Last, small differences in the yield surface curvature may have significant impact on strain localization and material ductility. Dæhli et al. (2017b) have shown that higher curvature generally lowers the failure strain. Since the rigorous porous plasticity model develops rounded triangular yield loci for certain stress states, it seems reasonable to assume that this can lead to increased material ductility compared to the heuristic porous plasticity model.

6.3. Influence of the RVE on the FE limit analyses

Since the hollow sphere model does not represent a periodic material structure, we find it interesting to examine the differences between a true periodic microstructure and the hollow sphere model. By true periodic microstructure, we refer to unit cell configurations that are space-filling. There exists a variety of true periodic microstructures. While a realistic periodic microstructure should take into account the underlying features of the real microstructure, a very simple RVE that is more computationally tractable, corresponds to a cubic unit cell with a uniform distribution of spherical voids. This section is devoted to comparisons between the cubic and the spherical unit cell models in terms of yield limits. We note that the comparison will be restricted to unit cells with a porosity level of $f = 0.01$, which suffices to highlight differences between the two types of RVE.

A mesh refinement study for the cubic unit cell model was conducted on beforehand to ensure converged results. We omit the details of the mesh convergence study, but note that the cubic unit cell model employed herein consists of 802 quadratic brick elements with reduced integration (C3D20R). The unit cell configuration then comprised 9 elements along the void edges, 10 elements along the intervoid ligament, and 8 elements on the outer edges. This spatial resolution was somewhat finer than what was found necessary for converged results to compensate for the limitations of the mesh refinement study in terms of imposed loading conditions and matrix yield function exponents. The two unit cell models employed in this section are shown in Fig. 19.

Plastic limit loads for $m = 2$, 8, and 20 are shown in Fig. 20. The stress triaxiality levels correspond to $T = 0$ (left column), $T = 1$ (middle column), and $T = 10$ (right column) for deviatoric angles $\Omega = 0^\circ, 5^\circ, \ldots, 60^\circ$ to highlight differences under various loading scenarios. These results show that the cubic unit cell model always provides lower plastic limit loads than the spherical model. This implies that plastic yielding of more realistic RVE types is likely to precede plastic yielding of the

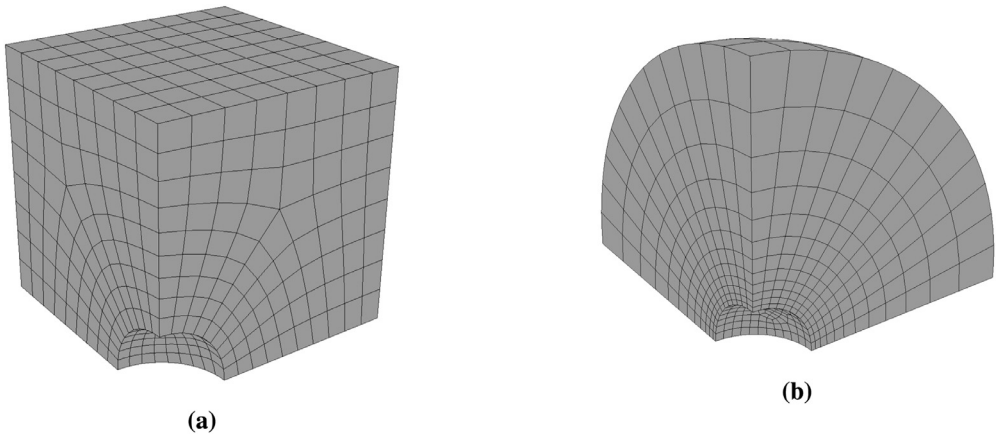

Fig. 19. Illustrations of the FE models for (a) the cubic RVE and (b) the spherical RVE.

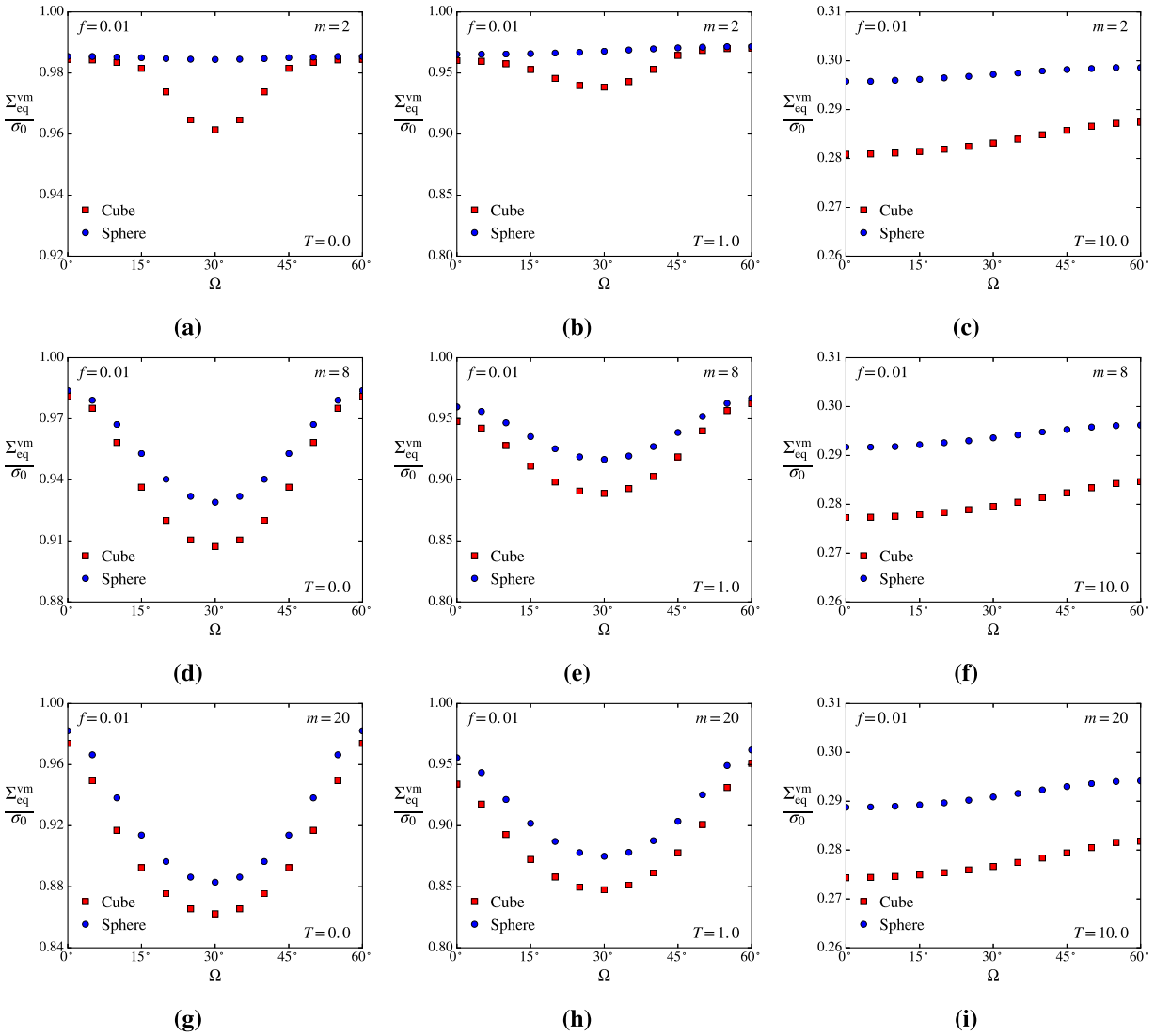

Fig. 20. Comparison between the yield limits from the FE analyses using a spherical (blue circle markers) or a cubic (red square markers) unit cell model with a porosity level of $f = 0.01$. Results are shown for $T = 0$ (left column), $T = 1$ (middle column), and $T = 10$ (right column) for the yield surface exponents $m = 2$ (top row), $m = 8$ (middle row), and $m = 20$ (bottom row). (For interpretation of the references to colour in this figure legend, the reader is referred to the web version of this article.)

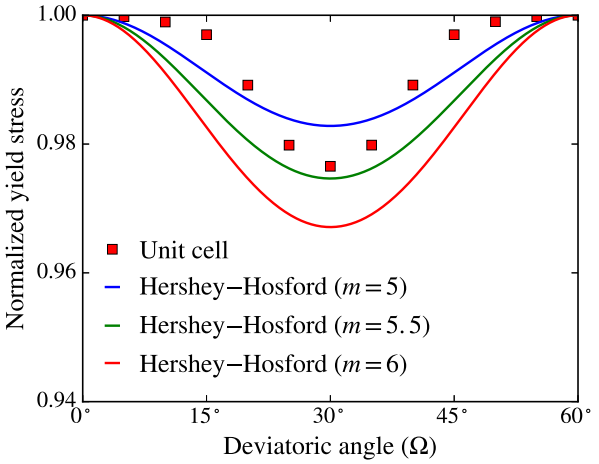

Fig. 21. Comparison of normalized yield stress against deviatoric angle between the FE limits points using the cubic RVE with $m = 2$ and the Hershey-Hosford yield function. The stress triaxiality of the unit cell data corresponds to $T = 0$, while the Hershey-Hosford yield function is independent of the stress triaxiality.

approximate hollow sphere model. Further, this observation is interesting because it implies that the Gurson-type models provide even higher upper-bound solutions for true periodic microstructures relative to the microstructure approximated by a hollow sphere. This gives impetus to the modification of the Gurson model by Tvergaard (1981), where the q_i parameters were introduced to obtain better agreement to plane strain bifurcation analyses. In light of the yield function defined by Eq. (20), and letting $q_3 = q_1^2$, the plastic limit loads under pure shear loading and pure hydrostatic loading correspond to

$$\Sigma_{\text{eq}} = (1 - q_1 f)\sigma_0 \qquad \text{for } \Sigma_{\text{h}} = 0 \tag{30a}$$

$$|\Sigma_{\text{h}}| = -\frac{2\sigma_0}{3q_2}\ln(q_1 f) \qquad \text{for } \Sigma_{\text{eq}} = 0 \tag{30b}$$

We readily perceive that, by for instance using the parameters proposed by Tvergaard (1981) with $q_1 = 1.5$ and $q_2 = 1$, the plastic limit loads will be reduced and consequently provide better predictions for true periodic microstructures. As such, the q_i parameters of the Gurson-Tvergaard model can be considered a means to adapt the yield function derived for a hollow sphere to a more realistic periodic microstructure, which in this context is associated with a cubic RVE.

While the shape of the yield curves are qualitatively similar for the two highest yield surface exponents ($m = 8$ and $m = 20$), in the sense that the yield loci for the cubic and spherical unit cell models have a similar appearance, the cubic unit cell model provides a rather different effect of the deviatoric angle (or equivalently J_3) on the plastic limit loads for the quadratic matrix yield surface ($m = 2$). This is readily observed for the stress triaxiality ratios $T = 0$ and $T = 1$ in Fig. 20(a) and 20(b), respectively. The shape of these curves, giving a minimum limit load under generalized shear loadings, bears resemblance to those of the Hershey-Hosford yield function ($m < 2$ or $m > 4$). Similar findings were reported by Keralavarma (2017). Thus, the macroscopic yield surface for the cubic RVE unit cell model governed by J_2 flow theory displays a qualitatively similar influence of the deviatoric stress state as that found for randomly oriented polycrystals (Bishop and Hill, 1951; Hosford, 1972; 1996; Hutchinson, 1964; Logan and Hosford, 1980). This is shown in Fig. 21 where the normalized yield stress is plotted against the deviatoric angle for the cubic RVE and the Hershey-Hosford yield criterion with different exponents. The stress triaxiality of the FE data corresponds to $T = 0$. We note that this observation only pertains to the low stress triaxiality ratios, and in particular to the zero triaxiality condition ($T = 0$). Although the yield locus of the cubic RVE model qualitatively displays similar behaviour as the underlying matrix formulation, the mechanism for the observed effect of the stress deviator is quite different from that of a polycrystal with a random texture governed by crystal plasticity theory.

7. Concluding remarks

Numerical limit analyses using an FE model of a hollow sphere RVE have been performed to examine the effects of a J_3-dependent matrix yield surface on the macroscopic yielding of a porous ductile solid. The matrix material was governed by the Hershey-Hosford yield criterion and three yield surface exponents were employed, corresponding to one quadratic ($m = 2$) and two non-quadratic matrix yield surfaces ($m = 8$ and $m = 20$). The numerical data were used to evaluate the influence of the macroscopic deviatoric angle (or equivalently J_3) on the macroscopic yielding of the porous ductile solid and further to assess the predictions of two different porous plasticity models. The first porous plasticity model is obtained from a rigorous upper-bound limit analysis (Benallal, 2017), while the second is a simple heuristic extension of the Gurson-Tvergaard model (Dæhli et al., 2017b).

The numerical limit analyses show that the macroscopic yield surface of the hollow sphere model transforms from the underlying matrix yield surface for zero hydrostatic stress to a rounded triangular shape in the deviatoric plane. When the hydrostatic stress is positive, the macroscopic yield surface attains a maximum value in generalized compression, whereas the macroscopic yield surface attains a maximum value in generalized tension for negative hydrostatic stress. Further, the macroscopic yield surfaces are found to be centro-symmetric, which is a general property for porous materials with a matrix yield criterion that is an even function of the stress tensor. For the quadratic matrix yield surface (i.e. $m = 2$), a monotonic increase/decrease of the macroscopic yield stress with the deviatoric angle (opposite between positive and negative hydrostatic stress due to centro-symmetry) is observed already for very low stress triaxiality ratios. For the non-quadratic matrix yield surfaces, the macroscopic yield surface attains a minimum yield limit around generalized shear up to rather high stress triaxiality levels, before the monotonic increase/decrease of the yield stress with the deviatoric angle becomes apparent. Note that even in the cases where the yield stress is minimized around generalized shear, the yield strength is different between generalized tension and compression and the centro-symmetry is prevalent. The shape transformation of the macroscopic yield surface was found to be highly influenced by the porosity level; high porosity facilitates earlier shift to a rounded triangular shape with six-fold symmetry. In the case of very high stress triaxiality ratios, e.g. $T \approx 10$, the yield loci corresponding to constant levels of stress triaxiality appear more or less circular in shape; thus, the effect of the third deviatoric stress invariant is diminishing for sufficiently high stress triaxiality ratios, regardless of the underlying matrix yield surface, and will eventually vanish in the hydrostatic limit.

Comparison of the two porous plasticity models to the FE limit analyses show that the rigorous upper-bound porous plasticity model gives accurate predictions for all stress states, porosity levels, and matrix yield surface exponents. The largest discrepancies were found for the highest porosity level in the case of purely deviatoric loading. The heuristic model retains the shape of the underlying matrix yield surface for yield loci corresponding to constant hydrostatic stress and is consequently incapable of describing the shape transformation of the macroscopic yield surface that is apparent both in the FE limit analyses and for the rigorous model. This gives marked differences for the highest porosity level ($f = 0.1$), especially for moderate and up to rather high stress triaxiality ratios. However, in the case of generalized shear loading, the predictions of the heuristic model are in close agreement to both the FE limit analyses and the rigorous model. The same conclusion holds for the two lower porosity levels ($f = 0.01$ and $f = 0.001$), for which the heuristic model gives reasonably good agreement to the FE limit analyses and the rigorous model for all stress states. Considering the simple formulation of the heuristic model, and the fairly good accuracy for realistic porosity levels, it is deemed a viable means to include first-order effects of J_3 into the porous plasticity modelling framework for structural applications. However, it is important to note that even though the heuristic model gives reasonable predictions of the yield stress, rather small discrepancies in the yield surfaces can be amplified for large deformations because the porosity evolution of the rigorous model and the unit cell calculations is affected by the J_3 stress invariant in addition to the hydrostatic stress. This can in turn cause larger differences for subsequent yield surfaces.

In the last section, we examined the difference between two types of RVE in the FE limit analyses, namely the hollow sphere model and a cubic model with a spherical void. These numerical results clearly show that the periodic RVE, represented by the cubic unit cell, lowers the plastic limit loads in the FE calculations. This implies that the predictions of both porous plasticity models are less accurate in comparison to a periodic RVE.

Acknowledgments

The authors gratefully appreciate the financial support from NTNU and the Research Council of Norway through the FRINATEK Programme, Project No. 250553 (FractAl). The SIMLab group (Structural Impact Laboratory) hosted at the Norwegian University of Science and Technology (NTNU) is gratefully acknowledged for providing the User Material (UMAT) subroutine needed to conduct the numerical analyses in this work.

References

Alves, J.L., Revil-Baudard, B., Cazacu, O., 2014. Importance of the coupling between the sign of the mean stress and the third invariant on the rate of void growth and collapse in porous solids with a von mises matrix. Model. Simulat. Mater. Sci. Eng. 22 (2), 025005. doi:10.1088/0965-0393/22/2/025005.

Barlat, F., 1987. Crystallographic texture, anisotropic yield surfaces and forming limits of sheet metals. Mater. Sci. Eng. 91, 55–72. doi:10.1016/0025-5416(87)90283-7.

Benallal, A., 2017. Constitutive equations for porous solids with matrix behaviour dependent on the second and third stress invariants. Int. J. Impact Eng. 108, 47–62. doi:10.1016/j.ijimpeng.2017.05.004.

Benallal, A., 2018. On some features of the effective behaviour of porous solids with J_2- and J_3- dependent yielding matrix behaviour. Comptes Rendus Mecan. 346 (2), 77–88. doi:10.1016/j.crme.2017.11.002.

Benallal, A., Desmorat, R., Fournage, M., 2014. An assessment of the role of the third stress invariant in the Gurson approach for ductile fracture. Eur. J. Mech. A/Solids 47, 400–414. doi:10.1016/j.euromechsol.2014.02.009.

Bishop, J.F.W., Hill, R., 1951. XLVI. A theory of the plastic distortion of a polycrystalline aggregate under combined stresses. Lond. Edinbu. Dublin Philosoph. Mag. J. Sci. 42, 414–427. doi:10.1080/14786445108561065.

Budiansky, B., Hutchinson, J.W., Slutsky, S., 1982. Void growth and collapse in viscous solids. In: Mechanics of Solids: The Rodney Hill 60th Anniversary Volume. Pergamon Press, London, pp. 13–46.

Cazacu, O., Chandola, N., Alves, J.L., Revil-Baudard, B., 2014a. Importance of the consideration of the specificities of local plastic deformation on the response of porous solids with tresca matrix. Eur. J. Mech. A/Solids 47, 194–205. doi:10.1016/j.euromechsol.2014.04.004.

Cazacu, O., Revil-Baudard, B., 2015. New three-dimensional plastic potentials for porous solids with a von mises matrix. Comptes Rendus Mécan. 343 (2), 77–94. doi:10.1016/j.crme.2014.12.001.

Cazacu, O., Revil-Baudard, B., Chandola, N., 2019. Plasticity-Damage Couplings: From Single Crystal to Polycrystalline Materials, 253. Springer.

Cazacu, O., Revil-Baudard, B., Chandola, N., Kondo, D., 2014b. New analytical criterion for porous solids with Tresca matrix under axisymmetric loadings. Int. J. Solids Struct. 51 (3–4), 861–874. doi:10.1016/j.ijsolstr.2013.11.010.
Cazacu, O., Revil-Baudard, B., Lebensohn, R.A., Gărăjeu, M., 2013. On the combined effect of pressure and third invariant on yielding of porous solids with von mises matrix. J. Appl. Mech. 80 (6), 1—-5. doi:10.1115/1.4024074.
Dæhli, L.E., Morin, D., Børvik, T., Hopperstad, O.S., 2018. A Lode-dependent Gurson model motivated by unit cell analyses. Eng. Fract. Mech. 190, 299–318. doi:10.1016/j.engfracmech.2017.12.023.
Dæhli, L.E.B., Faleskog, J., Børvik, T., Hopperstad, O.S., 2017a. Unit cell simulations and porous plasticity modelling for strongly anisotropic FCC metals. Eur. J. Mech. A/Solids 65, 360–383. doi:10.1016/j.euromechsol.2017.05.004.
Dæhli, L.E.B., Morin, D., Børvik, T., Hopperstad, O.S., 2017b. Influence of yield surface curvature on the macroscopic yielding and ductile failure of isotropic porous plastic materials. J. Mech. Phys. Solids 107, 253–283. doi:10.1016/j.jmps.2017.07.009.
Doege, E., Seibert, D., 1995. Prediction of necking and wrinkling in sheet-metal forming. J. Mater. Process. Technol. 50, 197–206.
Faleskog, J., Gao, X., Shih, C.F., 1998. Cell model for nonlinear fracture analysis – I. Micromechanics calibration. Int. J. Fract. 89 (4), 355–373. doi:10.1023/A:1007421420901.
Fritzen, F., Forest, S., Böhlke, T., Kondo, D., Kanit, T., 2012. Computational homogenization of elasto-plastic porous metals. Int. J. Plast. 29 (1), 102–119. doi:10.1016/j.ijplas.2011.08.005.
Guo, T.F., Faleskog, J., Shih, C.F., 2008. Continuum modeling of a porous solid with pressure-sensitive dilatant matrix. J. Mech. Phys. Solids 56 (6), 2188–2212. doi:10.1016/j.jmps.2008.01.006.
Gurson, A.L., 1977. Continuum theory of ductile rupture by void nucelation and growth: part I – Yield criteria and flow rules for porous ductile media. J. Eng. Mater. Technol. 99 (1), 2–15.
Hershey, A.V., 1954. The plasticity of an isotropic aggregate of anisotropic face-centered cubic crystals. J. Appl. Mech. 21 (3), 241–249.
Hosford, W.F., 1972. A generalized isotropic yield criterion. J. Appl. Mech. 39, 607–609.
Hosford, W.F., 1996. On the crystallographic basis of yield criteria. Textures Microstru. 26, 479–493. doi:10.1155/TSM.26-27.479.
Hutchinson, J.W., 1964. Plastic deformation of B.C.C. Polycrystals. J. Mech. Phys. Solids 12, 25–33. doi:10.1016/0022-5096(64)90004-3.
Keralavarma, S.M., 2017. A multi-surface plasticity model for ductile fracture simulations. J. Mech. Phys. Solids 103, 100–120. doi:10.1016/j.jmps.2017.03.005.
Kim, J., Gao, X., Srivatsan, T.S., 2004. Modeling of void growth in ductile solids: effects of stress triaxiality and initial porosity. Eng. Fracture Mech. 71, 379–400. doi:10.1016/S0013-7944(03)00114-0.
Koplik, J., Needleman, A., 1988. Void growth and coalescence in porous plastic solids. Int. J. Solids Struct. 24 (8), 835–853. doi:10.1016/0020-7683(88)90051-0.
Leblond, J.-B., Morin, L., 2014. Gurson's criterion and its derivation revisited. J. Appl. Mech. 81 (5), 1–7. doi:10.1115/1.4026112.
Lian, J., Chen, J., 1991. Isotropic polycrystal yield surfaces of B.C.C. and F.C.C. metals: crystallographic and continuum approaches. Acta Metallurgica et Materialia 39 (10), 2285–2294.
Liu, Z.G., Wong, W.H., Guo, T.F., 2016. Void behaviors from low to high triaxialities: transition from void collapse to void coalescence. Int. J. Plastic. 84, 183–202. doi:10.1016/j.ijplas.2016.05.008.
Logan, R.W., Hosford, W.F., 1980. Upper-bound anisotropic yield locus calculations assuming ⟨111⟩-pencil glide. Int. J. Mech. Sci. 22 (7), 419–430. doi:10.1016/0020-7403(80)90011-9.
Madou, K., Leblond, J.-B., 2012. A Gurson-type criterion for porous ductile solids containing arbitrary ellipsoidal voids - II: determination of yield criterion parameters. J. Mech. Phys. Solids 60, 1037–1058. doi:10.1016/j.jmps.2011.11.008.
Madou, K., Leblond, J.-B., 2013. Numerical studies of porous ductile materials containing arbitrary ellipsoidal voids - I: yield surfaces of representative cells. Eur. J. Mech. A/Solids 42, 480–489. doi:10.1016/j.euromechsol.2013.06.004.
Marciniak, Z., Kuczyński, K., 1967. Limit strains in the processes of stretch-forming sheet metal. Int. J. Mech. Sci. 9, 609–620. doi:10.1016/0020-7403(67)90066-5.
Nielsen, K.L., Dahl, J., Tvergaard, V., 2012. Collapse and coalescence of spherical voids subject to intense shearing: studied in full 3D. Int. J. Fract. 177 (2), 97–108. doi:10.1007/s10704-012-9757-4.
Pardoen, T., Hutchinson, J.W., 2000. Extended model for void growth and coalescence. J. Mech. Phys. Solids 48, 2467–2512. doi:10.1016/S0022-5096(00)00019-3.
Pastor, F., Pastor, J., Kondo, D., 2015. Numerical limit analysis and plasticity criterion of a porous coulomb material with elliptic cylindrical voids. Comptes Rendus Mecan. 343 (3), 199–209. doi:10.1016/j.crme.2014.12.004.
Pastor, J., Thoré, P., Pastor, F., 2010. Limit analysis and numerical modeling of spherically porous solids with coulomb and Drucker-Prager matrices. J. Comput. Appl. Math. 234 (7), 2162–2174. doi:10.1016/j.cam.2009.08.079.
Revil-Baudard, B., Cazacu, O., 2014a. New three-dimensional strain-rate potentials for isotropic porous metals: role of the plastic flow of the matrix. Int. J. Plast. 60, 101–117. doi:10.1016/j.ijplas.2014.04.003.
Revil-Baudard, B., Cazacu, O., 2014b. Role of the plastic flow of the matrix on yielding and void evolution of porous solids : comparison between the theoretical response of porous solids with tresca and von mises matrices. Mech. Res. Commun. 56, 69–75. doi:10.1016/j.mechrescom.2013.11.008.
Rice, J.R., 1976. The localization of plastic deformation. In: Proceedings of the 14th International Congress on Theoretical and Applied Mechanics, 1, pp. 207–220. 10.1.1.160.6740
Rice, J.R., Tracey, D.M., 1969. On the ductile enlargement of voids in triaxial stress fields. J. Mech. Phys. Solids 17 (3), 201–217. doi:10.1016/0022-5096(69)90033-7.
Soare, S.C., 2016. On the overall yielding of an isotropic porous material with a matrix obeying a non-quadratic criterion. Int. J. Eng. Sci. 104, 5–19. doi:10.1016/j.ijengsci.2016.04.005.
Søvik, O.P., Thaulow, C., 1997. Growth of spheroidal voids in elastic-plastic solids. Fatigue Fract. Eng. Mater. Struct. 20, 1731–1744. doi:10.1111/j.1460-2695.1997.tb01525.x.
Tekoğlu, C., Leblond, J.-B., Pardoen, T., 2012. A criterion for the onset of void coalescence under combined tension and shear. J. Mech. Phys. Solids 60, 1363–1381. doi:10.1016/j.jmps.2012.02.006.
Thoré, P., Pastor, F., Pastor, J., 2011. Hollow sphere models, conic programming and third stress invariant. Eur. J. Mech. A/Solids 30 (2), 63–71. doi:10.1016/j.euromechsol.2010.09.004.
Trillat, M., Pastor, J., 2005. Limit analysis and Gurson's model. Eur. J. Mech. A / Solids 24, 800–819. doi:10.1016/j.euromechsol.2005.06.003.
Tvergaard, V., 1981. Influence of voids on shear band instabilities under plane strain conditions. Int. J. Fract. 17 (4), 389–407. doi:10.1007/BF00036191.
Yi, S., Wang, D., 1989. A lower bound approach to the yield loci of porous materials. Acta Mech. Sinica 5 (3), 237–243.